Published in final edited form as:

Nature. 2021 June ; 594(7863): 448–453. doi:10.1038/s41586-021-03540-0.

Hippocampal AMPA receptor assemblies and mechanism of allosteric inhibition

Jie Yu[#1], **Prashant Rao**[#1], **Sarah Clark**[1], **Jaba Mitra**[2a,b], **Taekjip Ha**[2b,c,d,e], **Eric Gouaux**[1,3,*]

[1]Vollum Institute, Oregon Health & Science University, 3181 SW Sam Jackson Park Road, Portland, OR 97239

[2a]Department of Materials Science and Engineering, University of Illinois at Urbana-Champaign, Urbana, IL 61801

[2b]Department of Biophysics and Biophysical Chemistry, Johns Hopkins University, Baltimore, MD 21215

[2c]Department of Biophysics, Johns Hopkins University, Baltimore, MD 21215

[2d]Department of Biomedical Engineering, Johns Hopkins University, Baltimore, MD 21215

[2e]Howard Hughes Medical Institute, Baltimore, MD 21215

[3]Howard Hughes Medical Institute, Portland, OR 97239

[#] These authors contributed equally to this work.

Summary

AMPA-selective glutamate receptors mediate signal transduction between the neuronal circuits of the hippocampus[1]. Remarkably, the trafficking, localization, kinetics, and pharmacology of AMPA receptors are exquisitely tuned by an ensemble of auxiliary protein subunits, integral membrane proteins which associate with the receptor to yield *bona fide* receptor signaling complexes[2]. So far, extensive studies of recombinant AMPA receptor-auxiliary subunit complexes using engineered protein constructs have failed to faithfully illuminate the molecular architecture of hippocampal AMPA receptor complexes. Here we immunoaffinity-purify hippocampal, calcium-impermeable AMPA receptor complexes and utilize single molecule fluorescence and cryo-EM experiments to elucidate 3 major AMPA receptor-auxiliary subunit complexes. The GluA1/A2, GluA1/A2/A3, and GluA2/A3 receptors are the predominant assemblies, with the auxiliary subunits TARP-γ8 and CNIH2/SynDIG4 non-stochastically positioned at the B'/D' and A'/C' positions, respectively. We further demonstrate how the receptor:TARP-γ8 stoichiometry explains the mechanism and submaximal inhibition of a clinically relevant, brain-region specific allosteric inhibitor.

[*]Correspondence and requests for materials should be addressed to Eric Gouaux (gouauxe@ohsu.edu).

Author contributions

J.Y., P.R. and E.G. designed the project. J.Y. and P.R. performed the sample preparation for cryo-EM and biochemistry studies. J.Y. and P.R. performed the cryo-EM data collection, data analysis and model building. J.Y. performed the patch clamp recording experiments. S.C. performed all SimPull experiments with T.H and J.M. providing training and comments. E.G., J.Y., P.R., and S.C. wrote the manuscript with input from T.H. and J.M.

Competing financial interests

The authors declare no competing interests.

Introduction

Decades of studies have illuminated the central role played by ionotropic glutamate receptors (iGluRs) in fast excitatory signaling throughout hippocampal neuronal circuits[3] and in synaptic potentiation and depression[1,4]. One subfamily of iGluRs, deemed AMPA receptors, plays particularly important roles in the glutamatergic synapses of the hippocampus[1]. AMPA receptors are tetrameric assemblies[5–7], composed of subunits GluA1–4[8], with subunits GluA1–2 most abundantly expressed in the hippocampus[9,10]. AMPA receptors do not function in isolation, however, and co-assemble with auxiliary subunits that modulate trafficking, localization, kinetics, and pharmacology of the assembled receptor complex[2,11], further sculpting synaptic responses, synaptic plasticity and neuronal circuit activity.

The most prevalent auxiliary subunits in the hippocampus are transmembrane AMPA receptor regulatory protein gamma 8 (TARP-γ8)[12], cornichon-2 (CNIH2)[13], and synapse differentiation-induced gene 4 (SynDIG4)[9]. Despite nearly two decades since the discovery of the first AMPA receptor auxiliary subunit[14], the determination of the molecular and structural composition of hippocampal AMPA receptors (hpAMPARs) remains unknown. Prior studies revealed structures of the GluA1/GluA2-TARP-γ8 and GluA2-CNIH3 complexes[15,16], however, these experiments employed artificial, engineered recombinant proteins, leaving the question of the ensemble of AMPA receptor complexes of the hippocampus unresolved. Therefore, we isolated native, calcium-impermeable AMPA receptor complexes from mammalian hippocampi and utilized single particle cryo-EM and single-molecule total internal reflection fluorescence (TIRF) experiments[17] to define the functionally relevant molecular composition and structures of the most highly populated classes of hpAMPARs. With these native complexes in hand, we proceeded to elucidate the stoichiometry, pose, and mechanism of a clinically relevant, brain region selective antagonist, bound to its physiological, functional target.

Structure and composition of hpAMPARs

We isolated GluA2-containing hpAMPARs from mouse hippocampi, followed by immuno-subunit labeling with the anti-GluA1 11B8 single-chain variable fragment (scFv) and the GluA3 5B2 Fab (Extended Data Fig. 1a), with inclusion of the competitive antagonist MPQX and the TARP-γ8 specific antagonist, JNJ-55511118 (JNJ)[19]. The presence of GluA1-A4 subunits, PSD-95, TARP-γ8, and CNIH2 were confirmed by Western blot (Extended Data Figs. 1b, 2 and Supplementary Fig. 1), suggesting that our isolation procedure, which represents complexes derived from total receptor mass, had released synaptic AMPA receptor complexes from the PSD. We collected a large single particle cryo-EM dataset (Supplementary Table 1) and initial 2D classification revealed densities for the 11B8 scFv, the anti-GluA2 15F1 Fab, and the 5B2 Fab (Extended Data Fig. 1c–d) bound to their cognate receptor subunits. Two prominent density features extend from the transmembrane domain (TMD) ‘up’ along the sides of the ligand-binding domain (LBD) of the receptor, likely from the extracellular loops of TARP-γ8 (Extended Data Fig. 1d). Multiple rounds of ATD-focused classification and refinement revealed four distinct

hpAMPAR complexes adopting 'Y-shaped' symmetric or asymmetric conformations[5] (Fig. 1a–d, Extended Data Figs. 3–6).

The hpAMPAR complexes composed of GluA1 and GluA2 subunits are the predominant subtypes, present in ~90% of our structures (Fig. 1a–d), consistent with previous studies that GluA1 and GluA2 constitute ~80% of AMPAR subunit expression in the hippocampus [9,20,21]. Compared to the distribution in the whole brain, where the largest population of receptors is composed of the A1A2A3A2 subunit assemblies (GluA1/A2/A3)[18], our dataset analysis revealed that the A1A2A1A2 (GluA1/A2) receptor accounts for the largest population in the hippocampus (~56%), with the GluA1 subunit in the A/C positions and the GluA2 subunit in the B/D positions (Fig. 1a). The second major population is the GluA1/A2/A3 receptor, accounting for ~36% of the total population, with the GluA1, GluA3, and GluA2 subunits in A, C and B/D positions, respectively (Fig. 1b). The A1A2AXA2 and A3A2A3A2 complexes comprise ~4% of the population (Fig. 1c, d). The A1A2AXA2 receptor includes an 'AX' subunit, which we define as a subunit unlabeled by an antibody fragment either because a Fab/scFv has unbound or because it is the GluA4 subunit. The A3A2A3A2 (GluA2/A3) receptor is the only complex without the GluA1 subunit and similar to the subunit composition of the whole brain receptor population[18], GluA3 subunits reside in the A/C positions.

To independently assess the relative abundance of each subunit in the hippocampus, we performed single molecule pull down (SiMPull) experiments[17] by applying mouse hippocampal supernatant to imaging chambers coated with the 15F1 mAb (Fig. 1e). Fluorescently labeled antibodies specific for the GluA1, GluA3, or GluA4 subunits were then applied to the chamber to enable visualization of AMPAR subunits. We observed 60% more GluA1 molecules compared to GluA3 molecules, further demonstrating the prevalence of the GluA1 subunit in the hippocampus (Fig. 1e, Extended Data Fig. 7a). When fluorescently labeled anti-GluA1 and anti-GluA3 antibodies were simultaneously added to the imaging chamber, we saw 37% colocalization of GluA3 molecules with GluA1 (Fig. 1e). By comparing number of spots for each subunit to the total number of observed complexes, we determined that 77% of complexes contained GluA1, 30% contained GluA3, and 3% contained GluA4 by SiMPull (Fig. 1f, Extended Data Fig. 7b). A similar hpAMPAR subunit distribution is observed in the cryo-EM dataset, where 95% of complexes contained GluA1, 42% contained GluA3, and 4% contained GluAX (Fig. 1f). The percentage of non-tagged subunits observed in cryo-EM (4%) is close to the number of GluA4 subunits detected by SiMPull (3%), consistent with the hypothesis that the subunit unlabeled by an antibody fragment in the cryo-EM studies is the GluA4 subunit.

The GluA1/A2 and GluA2/A3 complexes adopt symmetric (S) and asymmetric (AS) conformations and the GluA1/A2/A3 complex adopts three different conformations[16] (Fig. 1a–c) (Extended Data Figs. 5, 6, 8). Inspection of the ATD-LBD interfaces shows that the closest contact regions between the ATD and LBD are conserved across these three complexes and involve a Tyr on the LBD, with a glycosylation site, a Lys and a Gln/Glu from the ATD. Tyr465 of GluA1 and Tyr469 of GluA3 may act as a 'pivot', transducing conformational signals from the ATD to the LBD. The observation that the ATD

glycosylation site densities nearly extend to the LBD may relate to the role of glycosylation in AMPA receptor physiology[22].

Constellation of auxiliary proteins

The hpAMPAR reconstructions revealed partial density for auxiliary proteins surrounding the receptor TMD. To improve the map quality, we performed focused classification and refinement for the GluA1/A2, GluA1/A2/A3, and GluA2/A3 receptor subtypes by masking the LBD-TMD layers (Extended Data Fig. 9). We conducted 3D classification individually for the three receptor subtypes and found that all of them exhibited density features consistent with an arrangement of two distinct pairs of auxiliary proteins (Extended Data Figs. 5–6). Refinement of the LBD-TMD layers for the GluA1/A2 subtype yielded a 3.63 Å resolution map (LBD-TMD$_{A1/A2}$) that permitted us to assign CNIH2 and TARP-γ8 to the identities of the auxiliary proteins at the A'/C' and B'/D' positions, respectively (Fig. 2a–b). Refinements of the GluA1/A2/A3 and GluA2/A3 subtypes resulted in reconstructions at lower resolution, but they nevertheless displayed similar auxiliary subunit densities as seen for the GluA1/A2 receptor (Extended Data Figs. 5–6).

To independently assess the identity and stoichiometry of the hpAMPAR auxiliary subunits, we performed SiMPull experiments using fluorescently-labeled antibodies and mouse hippocampal supernatant. The hpAMPARs were immobilized with the 15F1 mAb and probed for TARP-γ8 using a fluorescently-labeled anti-TARP-γ8 13A8 mAb in conjunction with anti-GluA1 and anti-GluA3 mAbs (Extended Data Fig. 7c). The resulting signal for TARP-γ8 colocalizes with GluA1 (65%) and GluA3 (38%), consistent with the conclusion that TARP-γ8 resides in the hpAMPAR complex (Fig. 2f). To measure the stoichiometry of TARP-γ8 in the hpAMPAR complex, we generated a GFP-tagged 13A8 Fab for use in single-molecule photobleaching experiments (Extended Data Fig. 7d). Approximately 69% of TARP-γ8 molecules bleached in two steps, 26% bleached in one step, and 5% bleached in three steps (Fig. 2g–h), consistent with most of the hpAMPAR complexes harboring two TARP-γ8 subunits. While we have not yet developed a CNIH2 antibody suitable for SiMPull experiments, the density is consistent with CNIH2 occupying the A'/C' auxiliary subunit positions.

TARP-γ8 is the most abundant auxiliary protein in the hippocampus[9,21,23], playing key roles in AMPA receptor gating, trafficking, basal expression, and long-term potentiation of hippocampal neurons[24–26]. TARP-γ8 occupies the 2-fold related, gating-dominant B'/D' positions (Fig. 2b), participating in extensive interactions with the M1 helix of the GluA1 subunit and the M4 helix of the GluA2 subunit[15]. The TM3 and TM4 helices of TARP-γ8 mediate the majority of interactions with the receptor TMD, with Tyr199 and Tyr201 forming hydrogen bonds with Glu520 of the GluA1 subunit (Fig. 2c). The TARP-γ8-ECD is poised near the lower lobes (D2) of receptor-LBD interdimer interfaces between subunits A/B and C/D, regions of the receptor involved in receptor gating and desensitization[27,28].

CNIH2 is abundant in the hippocampus, increases the surface expression of AMPARs[13,29,30], regulates AMPAR pharmacology[25,31], and slows the time course of excitatory postsynaptic currents (EPSCs)[30,32]. We observe CNIH2 occupying the A'/C' positions within the receptor TMD, at the second pair of auxiliary protein 'slots' flanking the

M1 and M4 receptor helices, with TM1 and TM2 extending 25 Å into the cytosol (Fig. 2d). Interactions between CNIH2 and the receptor TMD primarily involve two sites located at the extracellular and cytosolic boundaries of the TMD. At the extracellular boundary Phe3, 5, and 8 of CNIH2 form hydrophobic contacts with residues on the GluA2 M1 helix and on the GluA1 M4 helix (Fig. 2d). At the cytosolic interface, Phe22 and Trp26 of CNIH2 make contacts with Leu807 and Phe810 on the GluA1 M4 helix (Fig. 2d). We observe additional points of contact at the cytoplasmic boundary, where a lipid molecule bridges residues Val69 and Ser73 from TM2 with Ile573 on the pore-forming GluA2 M2 helix.

We next sought to compare our LBD-TMD_{A1A2} structure with the recently reported, recombinant GluA2-CNIH3 structure[16]. Analysis of the LBD layer shows that while each LBD dimer is similar, the two dimers are displaced relative to one another by about 3.2 Å (Extended Data Fig. 10). Superimposing the TMD layers revealed larger differences, with an overall RMSD of 3.3 Å (see Methods). Not only are the M1, M3, and M4 helices for the GluA2-CNIH3 structure rotated by 7–9^{o} relative to the equivalent helices in the LBD-$TMD_{A1/A2}$ structure, but the helices are also ‘compressed’ and shifted toward the central axis (Extended Data Fig. 10). Accordingly, the auxiliary subunits are also rotated and compressed towards the central axis (Extended Data Fig. 10). These differences suggest that the GluA2-CNIH3 structure may represent a non-native or immature conformation.

The stoichiometry of CNIH2 and TARP-γ8 offers an opportunity to examine how their positional arrangement is associated with AMPAR functional properties. CNIH2 and TARP-γ8 occupy the A’/C’ and B’/D’ positions, respectively. Because both pairs of positions permit direct interaction with the receptor M1 and M4 helices, we superimposed the A’ and B’ positions. As opposed to the TARP-γ8-receptor interface, inspection of the upper portion of the M1 helices revealed a 5.5° rotation away from the ion channel at the CNIH2-receptor interface (Fig. 2e). In addition, there is a 3.3^{o} rotation of the M3 helix that results in expansion of the gating-proximal region of the M3 helix (Fig. 2e). Thus, CNIH2 occupancy of the A’/C’ positions promotes an expansion of the receptor TMD, and defines one structural mechanism by which auxiliary protein occupancy may influence channel gating. Furthermore, superimposition of the recombinant GluA1/A2-TARP-γ8 structure with our LBD-$TMD_{A1/A2}$ structure shows the A’/C’ positions are shifted closer to the central axis when occupied by CNIH2 (Extended Data Fig. 10).

Interactions between the receptor and auxiliary subunit TM domains may also influence the conserved arrangement of auxiliary subunits around the receptor TMD. From our LBD-$TMD_{A1/A2}$ structure, we determined that CNIH2 and TARP-γ8 both participate in extensive interactions with the receptor M1 and M4 helices. Therefore, we explored the possibility that subunit specificity from the GluA1/GluA2 receptor directly influences auxiliary protein arrangement. Even though the sequences of the M1 and M4 helices are highly conserved between the GluA1 and GluA2 subunits, there is a single difference located in the middle of the M4 helix: Ile796 of GluA1 and its equivalent in GluA2, Val800. At the A’/C’ positions, Ile796 is poised to interact with residues Met11, Leu12, and Val15 of TM1 from CNIH2. Conversely, the residues surrounding Val800 are Leu170, Ile173, and Ile174 from TM3 of TARP-γ8. Interestingly, we resolved the same two-fold auxiliary protein stoichiometry from the GluA1/A2/A3 subtype (Extended Data Fig. 6), where the equivalent residue from the M4

helix of GluA3 harbors a Val. Thus, the sequence differences in the M4 helix may not be the only mechanism defining auxiliary protein occupancy.

The resolution of the LBD-$TMD_{A1/A2}$ map enabled us to visualize native lipid densities and the side-chain orientations at the amino acid positions dependent upon RNA editing. Lipid densities (Fig. 2a) are predominantly located between TARP-γ8 and CNIH2, near the M1 and M2 helices and do not occlude the ion permeation pathway, different from the locations of lipids in recombinant structures[16]. The lipid locations suggest they may harbor a functional role in receptor assembly or function. At the apex of the selectivity filter, there is clear density for Gln582 and Arg586 at the Q/R sites for GluA1 and GluA2, respectively (Extended Data Fig. 11a–b). Visualization of Arg586[33], projecting 'upward' into the central vestibule, illustrates how charged repulsion dictates ion selectivity[34], single-channel conductance[35], and resistance to cytoplasmic polyamines[36]. Within the LBD, RNA editing at the R/G sites[37] modulates the kinetic properties of AMPARs. We assigned Arg739 and Arg743 to the R/G sites for GluA1 and GluA2, respectively, based on density for the side chains (Extended Data Fig. 11a–b), suggesting that the majority of the isolated GluA1/GluA2 receptors contributing to our LBD-$TMD_{A1/A2}$ map would exhibit the fast kinetics associated with the R variants.

Mechanism of JNJ antagonism

JNJ, a brain region specific TARP-γ8 dependent AMPA receptor antagonist[19], incompletely inhibits steady state current evoked by saturating glutamate (Fig. 3c–d). We discovered 2-fold related densities of JNJ poised at each side of the interfaces between TARP-γ8 and GluA1 (Figs. 2b–c, 3a). The benzimidazolinone group of JNJ is wedged in between TM3 and TM4 of TARP-γ8 while the fluoro group points toward the M1 helix of GluA1, consistent with the predicted binding pose[19]. Extensive interactions are formed between JNJ and the surrounding residues, including possible hydrogen bonds and polar interactions between the benzimidazolinone group and the backbone carbonyl groups of Gly208 and Asn172 of TARP-γ8, and between the fluoro group and Cys524 of GluA1. In addition, the benzene group of the JNJ molecule is sandwiched between Phe205 of TARP-γ8 and Phe527 of GluA1 (Fig. 3a–b). Binding of JNJ expands a cavity at the interface of TARP-γ8 and GluA1, inducing an 'inward' rotation of the M1 helix and increasing distances between surrounding residues to prevent clashes with TM3–4 of TARP-γ8 and M1 of GluA1, in accord with studies that proposed the unoccupied binding pocket is too small to allow the binding of drugs targeting TARP-γ8[15]. We speculate that JNJ antagonizes receptor gating by precluding the expansion of the M3 gating helices and the 'outward' movement of the M1 helices, thereby negatively modulating receptor function. Moreover, because there are only two binding sites, the GluA2 M3 helices are less constrained by JNJ binding and may be able to expand the 'gating ring', thus enabling partial opening of the ion channel gate, leading to incomplete receptor inhibition.

Previous studies have determined that mutations of several TARP-γ8 residues surrounding the JNJ binding site reduced the potency of JNJ [19]. Nevertheless, several residues from GluA1 and TARP-γ8 also interact with or are near the JNJ molecule and yet have not been examined. We thus mutated these residues to alanine and carried out electrophysiology

studies, showing that the M523A, C524A, and F527A mutants of GluA1 and the F205A mutant of TARP-γsubstantially diminished the efficacy of JNJ-induced reduction of glutamate-induced currents. The effects were especially profound for the GluA1-F527A/TARP-γ8 and GluA1/TARP-γ8-F205A mutants (Fig. 3e, Extended Data Fig. 12) and thus are in harmony with these residues playing key roles in the binding and activity of JNJ.

Putative SynDIG4 interaction sites

The LBD-$TMD_{A1/A2}$ map shows additional density features surrounding the receptor and auxiliary proteins that could not be assigned to lipids or other small molecules. To increase the resolution of the density map, we rationalized that combining all the receptor subtypes and using signal subtraction to remove the ATD layer and antibody fragments would yield a higher resolution map, knowing that the amino acid sequences of AMPA receptor subunit TMDs are highly conserved. Indeed, this image processing strategy (see Data processing strategy #2) yielded a map at 3.25 Å resolution, deemed the LBD-TMD_{mix} map (Extended Data Figs. 6, 11c–d, 13). The LBD-TMD_{mix} map displays the same subunit arrangement and auxiliary protein composition as observed in the LBD-$TMD_{A1/A2}$ map, except that a mixture of GluA1, GluA3, and GluA4 ($GluA_{mix}$) occupy the A/C positions (Fig. 4a). Remarkably, observed density features associated with arginine residues at the R/G and Q/R sites of GluA2 and $GluA_{mix}$ subunits remain consistent with extensive RNA editing (R in the GluA2-A4, R/G site) in the hippocampus. Additionally, the LBD-TMD_{mix} map enabled us to augment the trace of the CNIH2 TM3-TM4 loop, which is proximal to the crucial M1-M2 linker of the receptor. We also observe prominent lipid-like densities that we modeled as lipid alkyl chains, and found that the lipid positions differ from those determined in the recombinant receptor-auxiliary protein complexes, in that they are poised to contact the M1 and M4 helices or reside near the pore-lining M2 helix (Fig. 4a, d). In addition, there are several lipids surrounding the TMs of TARP-γ8 and CNIH2.

We also observe an unknown 2-fold related, helix-like density oriented nearly parallel to the M4 helix of GluA1 and located in a crevice at the interface of GluA1 and CNIH2 subunits (Fig. 4d). The shape and location of the unknown density led us to hypothesize that it was an additional auxiliary hpAMPAR protein. SynDIG4, also known as Proline-rich transmembrane protein 1 (PRRT1), is an AMPAR-associated protein that is enriched in the hippocampus[9], associates with TARP-γ8 and CNIH2, co-localizes with GluA1 and is predicted to have at least one transmembrane domain[38,39]. To determine if SynDIG4 co-purified with the hpAMPAR complex, we carried out SiMPull and fluorescent-detection, size exclusion chromatography (FSEC) experiments using a well characterized anti-SynDIG4 mAb[38]. In the SiMPull experiments, we observed a signal when immobilized hpAMPAR complexes were probed with a fluorescently-labeled anti-SynDIG4 mAb (Fig. 4b and Extended Data Fig. 7e). The spots corresponding to SynDIG4 exhibit 61% co-localization with TARP-γ8, suggesting that they are located in the same hpAMPAR complexes (Fig. 4b). Furthermore, FSEC experiments using the same fluorescently-labeled mAbs demonstrate that the AMPAR-TARP-γ8 complex can be shifted by the anti-SynDIG4 mAb, thus proving that SynDIG4 is associated with the hpAMPAR complex (Fig. 4b). Our data suggests that the unknown density is SynDIG4, although further experiments are required to unambiguously show that it is not another auxiliary subunit. Nevertheless, we

note that the putative SynDIG4 transmembrane domain is arranged approximately parallel to the TM helices of the receptor, making extensive contacts with the M4 helix of GluA1 and the TM1/4 helices of CNIH2 (Fig. 4a, c). The location of SynDIG4, on the periphery of the hpAMPAR complex, is consistent with it playing roles in receptor trafficking and localization and less of a role in receptor gating[39,40].

The molecular structures of hpAMPAR complexes reveal rules for receptor subunit and auxiliary protein assembly and the binding site of the clinically relevant TARP-γ8 antagonist, JNJ. GluA1 is the most prevalent subunit assembled in the GluA2-containing hpAMPAR complex, highlighting the important roles of GluA1 and GluA2 in synaptic transmission. The GluA1/GluA2 complex and the recently discovered GluA1/A2/A3 receptor are the major assemblies harboring the GluA2 subunit exclusively at the B/D positions, while the A/C positions are more permissive, suggesting that differential insertion of GluA1 or GluA3 subunits at the A/C positions is a mechanism of synaptic tuning. We further showed a conservation of auxiliary subunit composition and assembly for the GluA1/GluA2, GluA2/GluA3, and GluA1/GluA2/GluA3 complexes, with TARP-γ8 and CNIH2 occupying the B'/D' and the A'/C' positions, respectively. The well-resolved density from the GluA1/A2 LBD-TMD structure defines the position of crucial residues that modulate the permeation and gating of the receptor, including RNA-editing dependent amino acid variations. Notably, we further uncovered how JNJ binds to the TARP-γ8-receptor interface and stabilizes the receptor in a closed state, thus demonstrating that structure-based design of small molecules is feasible using the *bona fide* native receptor target. SynDIG4 assembles on the periphery of the TMD, interacting extensively with CNIH2, consistent with its primary role in modulating receptor trafficking and localization. The native hpAMPAR complexes obviate the bias of artificial, engineered complexes and show how the functional properties of AMPA receptors are sculpted by the non-stochastic assembly of receptor and auxiliary protein components.

Methods

Expression and purification of anti-GluA1 11B8 scFv

The DNA sequences encoding the light and heavy chains of the variable domains of the GluA1-specific 11B8 monoclonal antibody (mAb), with the following modifications, were cloned into the pET-22b vector for expression in *Escherichia coli* BL21 cells. A hydrophilic linker, $(SGGGG)_3$, was employed to connect the light chain (V_L) and heavy chain (V_H), and an N-terminal pelB signal peptide and a C-terminal Strep II tag were also introduced into the construct. Cells were grown at 37°C in Terrific Broth containing 100 μg/ml ampicillin. Expression of the 11B8 scFv was induced by addition of 0.1 mM isopropyl β-D-1-thiogalactopyranoside (IPTG) when OD_{600} reached 1.5~1.8. The temperature of the cultures was reduced to 25 °C and the cells were gown for another 20 hr. Cells were harvested by centrifugation and lysed by osmotic shock in a lysis buffer containing 200 mM Tris, pH 8.0, 20% sucrose and 1 mM EDTA for half hour on ice. Centrifugation at 200,000 g, for 1 hour at 4 °C, was carried out to separate periplasmic proteins from cells and cell debris. The supernatant was dialyzed thrice against 2 liters of TBS buffer (20 mM Tris, pH 8.0 and 150 mM NaCl) at 4 °C to remove sucrose. The 11B8 scFv was purified by Strep-Tactin affinity

chromatography and the eluted protein was subjected to size-exclusion chromatography (SEC) using a Superdex 75 10/300 column equilibrated with TBS buffer. Peak fractions corresponding to monomeric 11B8 scFv were pooled and stored at −80 °C. Concentrated 11B8 scFv without any dilution were used for structural determination experiments.

Expression and purification of anti-GluA2 15F1 Fab

The DNA sequences encoding the Fab domains of the light and heavy chains from the GluA2-specific 15F1 mAb were cloned into a bicistronic pFastBac1 vector for baculovirus expression in Sf9 insect cells, with the following modifications[41]. The GP64 signal peptide (MVSAIVLYVLLAAAAHSAFA) was included at the N-terminus of the heavy and light chains, while a Strep II tag was introduced at the C-terminus of the heavy chain. Insect cells were transduced with baculovirus and cultured at 27 °C. After 96 hours, the supernatant was collected and the pH was adjusted to 8.0, followed by clarification at 10,000g for 20 min at 4 °C. The supernatant was concentrated to ~200 ml by tangential flow filtration using a 30 kDa MW cutoff filter and dialyzed thrice against TBS buffer for 36 hr. Strep-Tactin affinity chromatography was used to isolate the 15F1 Fab, which was further purified by SEC in the presence of TBS buffer. Peak fractions were pooled and stored at −80 °C. Concentrated 15F1 Fab without any dilution were used for structural determination experiments.

Purification of anti-GluA3 5B2 mAb and Fab

The GluA3-specific mAb (5B2) was purified from hybridoma supernatant by Protein A agarose chromatography. To produce the Fab fragment, the 5B2 mAb was digested by papain (1:30 w/w ratio) along with 5 mM cysteine and 1mM EDTA for 2.5 hr at 37 °C. The reaction was stopped by 30 mM iodoacetamide for 20 min in the dark. Fc fragments were removed by protein A agarose chromatography and the ‘flow through’ Fab fraction was collected and subjected to SEC in TBS buffer. Peak fractions were pooled, concentrated and stored at −80 °C. Concentrated 5B2 mAb without any dilution were used for structural determination experiments.

Generation of anti-GluA4 antibody

A mouse GluA4 construct (Uniprot code: Q9Z2W8) was engineered by addition of a C-terminal Strep II tag and deletion of largely unstructured C-terminal residues after Lys848, and was cloned into a pEG BacMam vector for baculovirus-mediated expression in mammalian cells[42]. The receptor was expressed in virally transduced HEK293S GnTI (−) cells and purified by Strep-Tactin affinity chromatography and SEC in TBS buffer supplemented with n-dodecyl-B-D-maltopyranoside (DDM). As previously described[43], the purified GluA4 protein was reconstituted into lipid A containing liposomes for mouse immunization and antibody production. Subsequently, candidates were screened by FSEC[44] and Western blot, and binding affinities were determined by bio-layer interferometry using an OctetRED384 instrument. We identified one mAb produced by the E3 hybridoma cell line that binds to a tertiary epitope of GluA4 with a K_D of 13 nM. To examine cross-reactivity of E3 mAb with other AMPARs, we carried out FSEC experiments using GluA1-mKalama, GluA2-GFP and GluA3-GFP tagged receptors, and determined that the E3 mAb is specific for the GluA4 receptor.

Generation and expression of anti-TARP-γ8 antibody

The mouse TARP-γ8 protein (Uniprot code: Q8VHW2) was modified by an addition of a C-terminal Strep II tag. DNA encoding this construct was cloned into a pEG BacMam vector for expression in HEK293S GnTI (−) cells through baculovirus transduction[42]. Strep-Tactin affinity chromatography and SEC were carried out to purify TARP-γ8 in TBS buffer supplemented with 0.5 mM DDM. Purified TARP-γ8 was reconstituted into lipid A-containing liposomes for mouse immunization and antibody production, as described previously. Secreted antibodies from the subsequent positive hybridoma clones were screened by FSEC [44] and Western blot, and affinities were determined by Octet measurements. We identified a Western positive mouse mAb produced by the 13A8 hybridoma cell line with a K_D of 1 nM. Cross-reactivity of the 13A8 mAb with other members of the TARP family was investigated by FSEC using TARP-γ2-GFP, TARP-γ3-GFP, TARP-γ4-GFP and TARP-γ7-GFP tagged proteins. We observed no cross-reactivity and found the 13A8 mAb is specific for TARP-γ8.

The DNA sequences encoding the 13A8 Fab domains of the heavy and light chains were derived from hybridoma cell mRNA via PCR amplification and were cloned into a biscistronic pFastBac1 vector. GP64 signal peptides were included at the N-terminus of the heavy and light chains, while a GFP tag was introduced to the C-terminus of the heavy chain, followed by a twin-Strep II tag. Expression and purification strategies were the same as those employed for the 15F1 Fab.

Isolation of native hippocampal AMPA receptors

Native hippocampal AMPA receptors were isolated from 200 C57BL/6 male and female mice (Charles River), aged 28–42 days. Mouse brains were dissected and immediately placed in ice-cold TBS buffer before dissection. Before isolating hippocampi, a clean razor blade was used to remove cerebella by cutting along the junction to the cerebral cortex, followed by hemisecting the left brain. The cortical hemisphere was peeled away[45] by placing two microspatula tips over the occipital cortex to expose the hippocampus. Subsequently, one spatula tip was used to anchor the brain and another spatula tip was positioned under the caudal tip of hippocampus. The hippocampus was then ‘scooped out’ by lateral movement of the second spatula tip. The collected hippocampi were immediately placed in ice-cold TBS buffer in the presence of 0.8 μM aprotinin, 2 μg/ml leupeptin, 2 mM pepstain A, 1 mM phenylmethylsulfonyl fluoride, 2 μM MPQX ([[3,4-dihydro-7-(4-morpholinyl)-2,3-dioxo-6-(trifluoromethyl)-1(2*H*)-quinoxalinyl]methyl]phosphonic acid) and 2 μM JNJ-55511118 (5-[2-chloro-6-(trifluoromethoxy)phenyl]-1,3-dihydro-2H-benzimidazol-2-one), homogenized using a Teflon-glass grinder and further disrupted by brief sonication, using a sonicator equipped with a tip size of 1.27 cm, for 5 min with 3 s on and 6 s off, at medium power, on ice. The membrane fraction was collected by ultracentrifugation at 200,000 g for 1 h at 4 °C. The crude membranes were solubilized in 2% (w/v) digitonin for 3 hours with slow stirring at 4 °C. The resulting solution was clarified by ultracentrifugation, and the supernatant was collected and mixed with excess Strep-tagged 15F1 Fab before passing through a Strep-Tactin affinity column by gravity flow. After washing the column extensively using buffer A (20 mM Tris, pH 8.0, 150 mM NaCl, 0.075 (w/v) digitonin, 2 μM MPQX and 2 μM JNJ-55511118), the complex of 15F1-

bound GluA2-containing receptor and excess 15F1 were eluted by buffer A supplementedwith 5 mM D-desthiobiotin. The eluted sample was incubated with an excess of 11B8 scFv and 5B2 Fab on ice for 30 min, concentrated, and further purified using a Superose 6 10/300 GL column in the presence of buffer A. Peak fractions were pooled and concentrated using a 100 kDa cut-off concentrator to an OD_{280} of 5 mg/ml for biochemical analysis and cryo-EM studies.

Cryo-EM sample preparation and data acquisition

A 2.5 μL aliquot of purified native hippocampal receptor complexes was applied to glow-discharged Quantifoil 2/1 200 mesh gold holey carbon grids which were blotted for 3 s under 100% humidity at 12 °C. The grids were flash-frozen in liquid ethane, using a FEI Mark IV cryo-plunge instrument.

Cryo-EM data was collected on a 300 kV FEI Titan Krios microscope operated in correlated double sampling (CDS) mode. Images were acquired on a K3 Summit direct-detector (Gatan) at a magnification of 29,000x, corresponding to a pixel size of 0.4027 Å/pixel in super-resolution mode. Images were collected using 'multi-shot' and 'multi-hole' methods customized in SerialEM[46], permitting acquisition of six movies per hole, from nine neighboring holes (3 × 3) per stage shift. Nominal defocus values ranged from −1.2 μm to −2.0 μm. Each raw movie stack consists of 60 frames, collected at a dose rate of ~6.8 e^-/pixel/s, for a total exposure time of 4.7 s resulting in a total dose of 50 $e^-/Å^2$ (Supplementary Table 1).

Image processing

We collected 46,927 super-resolution movies that were binned to a pixel size of 0.8055 Å/pixel. Beam-induced motions were corrected by patch motion correction (multi), and contrast transfer function (CTF) parameters were estimated by patch CTF estimation (multi) using cryoSPARC v2.14[47]. Two image distinct processing strategies, deemed #1 and #2, were conducted in parallel.

Data processing strategy #1.—Blob picker in cryoSPARC was used to pick particles from ~7,000 micrographs to generate 2D class averages with clear receptor features. A subset of these class averages was then used as templates for template-based picking from all 46,927 micrographs. Particles were extracted and downsampled to a box size of 128 × 128 pixels and subjected to several rounds of 2D classification. Only classes showing clear receptor features were kept, which resulted in retention of 2,893,667 particles. Next, 3D classification was performed in RELION 3.0[48], using a sampling interval of 15 degrees without masking or imposed symmetry, yielding three classes (1a, 1b, and 1c) displaying canonical receptor features with two 15F1 Fabs in the B/D positions and two 11B8 scFvs in the A/C positions at the ATD layer. Particles from classes 1b and 1c were combined and refined, while particles from class 1a were flipped 180º along the x axis to correct for an "upside down" orientation, before being refined separately. Particles from these two refinements (1b+c, 1a) were separately re-centered and re-extracted at a box size of 256 × 256. The two re-centered particle sets were classified into 10 and 12 classes, respectively. Classes displaying receptors labeled with the same antibody fragment densities were

combined into a single particle stack and subjected to another round of classification. From this round of classification, we sorted receptors bound with same Fab/scFv combination into two separate orientations of the ATD layer: symmetric (S) and asymmetric (AS). Particles from this round of classification were sorted into 6 groups based on the ATD labelling and orientations: A1A2A1A2-S, A1A2A1A2-AS, A1A2A3A2-AS1, A1A2A3A2-AS2, A1A2A3A2-AS3, A3A2A3A2-S and A3A2A3A2-AS.

We combined classes with the same ATD labeling and orientation and performed ATD-focused classification without any symmetry imposed on each group. For the A1A2A1A2-S class, the ATD layer was sub-classified into eight classes, of which one class occupying the largest population (55%) had the least well resolved secondary structure features. Another round of ATD focused classification was performed on this class, producing an A1A2AXA2 subtype, where “X” represents the subunit that was not labeled by any of the antibody fragments. From the remaining classes, three classes showing the most well-defined secondary structure features were selected for final refinement with C2 symmetry using cryoSPARC[49], producing a map at a global resolution of 4 Å. To improve map density in the ATD, we carried out ATD-focused refinement with C2 symmetry and obtained an ATD-A1A2A1A2-S map at a resolution of 3.4 Å. The same procedures were performed on classes corresponding to the other subtypes, with the exception that C2 symmetry refinement was only imposed on the A3A2A3A2-S group.

Data processing strategy #2.—All image processing was performed in cryoSPARC [47]. Motion-corrected, dose-weighted micrographs were curated by eliminating micrographs exhibiting imaging defects including excessive drift, broken holes or CTF estimation worse than 10 Å, resulting in 44,419 micrographs for further processing. Blob picker was used on a small subset of the data to generate 2D templates with distinguishable receptor features. These 2D templates comprised of a range of orientations and were used for interactive and automated particle picking using template-based picking. This resulted in 6,002,517 putative particles, which were initially extracted in a 256 × 256 box.

To remove images of ice, carbon support, and other debris, 2D and 3D classification were used to sort particles. First, 3D classification without masking or symmetry was implemented to sort particles. Two rounds of 3D classification were used to remove featureless particles by keeping only classes with discernible receptor features. This strategy was used to retain the maximum number of ‘good’ particles so that receptor subtypes with low populations could be resolved in subsequent processing steps. After sorting by 3D classification, 4,523,669 particles remained. This particle stack was then subjected to two rounds of reference-free 2D classification to eliminate poorly resolved particles, and resulted in a stack of 1,844,956 particles.

To resolve different receptor subtypes, the stack of 1,844,956 particles was subjected to multiple rounds of 3D classification. First *ab initio* 3D reconstruction was performed in cryoSPARC[47] without symmetry imposed to generate maps of several different AMPAR subtypes. These maps were used as initial references in order to sort particles by subtype using heterogenous refinement in cryoSPARC[47]. Multiple rounds of 3D classification were conducted, each time using maps from the previous run as new initial models. This allowed

for separation of receptor subtypes, as well as sub-classification of symmetric (S) and asymmetric (AS) receptors within these subtypes. Receptor subtypes were distinguished based on inspection of the ATD layer using the visualization and orientation of the 11B8 scFvs and the 15F1/5B2 Fabs. This strategy resulted in elucidation of six different subtypes, A1A2A1A2 (S/AS), A3A2A3A2 (S/AS), and A1A2A3A2 (AS1/AS2). Interestingly, processing strategy #2 did not uncover the A1A2AxA2 or the A1A2A3A2-AS3 subtype. This was because focused classification of the ATD layer was not utilized, and therefore unlikely to separate and resolve these low populated classes. We suspect that with data processing strategy #2, particles corresponding to these two subtypes are mixed within the other classes. Nevertheless, the percentages of particles of all of the remaining 3D classes and associated receptor subtypes were approximately the same for both processing strategies (Supplementary Table 2).

In all of the maps solved for the full receptor complexes, density in the LBD-TMD region was much weaker compared to the ATD layer. Therefore, using the maps solved from Strategy #1, we used focused classification of the LBD-TMD layer for each AMPAR subtype to improve the resolution of this region. Examination of the A1A2A1A2-S/AS maps revealed the same LBD-TMD stoichiometry and secondary structure. Therefore we performed focused 3D classification on particles combined from both conformations. Using a soft mask around the LBD-TMD layer and imposing C2 symmetry, classification in RELION 3.0 [48] resulted in three classes (classes 1, 7, and 8) that displayed continuous transmembrane helical densities. Classes 1 and 8 were selected for further classification focused on the LBD-TMD layer. Classes with strong density for the transmembrane domain and auxiliary proteins were combined for a final refinement in cryoSPARC[49], resulting in a map of the LBD-TMD layer at a resolution of 3.63 Å by the gold-standard FSC (0.143). In this map, auxiliary protein densities in the B'/D' positions show prominent extracellular protrusions that were well fit by TARP-γ8 (PDB Code: 6QKC) while densities in the A'/C' positions displaying minimal extracellular features were well fit by cornichon homolog 3 (CNIH3, PDB code: 6PEQ). We note that TARP-γ 2, -γ 3 and - γ 4 are also present in the hippocampus and speculate that we did not isolate a substantial number of these complexes because the JNJ compound specifically stabilizes the TARP-γ8 complex. We then performed the same focused classification procedure on the LBD-TMD layers of the A1A2A3A2 and A3A2A3A2 maps from strategy #1. First, C1 symmetry was imposed on the LBD-TMD-A1A2A3A2 map, followed by refinement with either C1 or C2 symmetry, yielding two maps at a resolution of 4.8 Å and 4.0 Å, respectively. The refined LBD-TMD-A1A2A3A2 maps, with either C1 or C2 symmetry, displayed the same auxiliary protein stoichiometry as that of the LBD-TMD-A1A2A1A2 complex, with two TARP-γ8 proteins in the B'/D' positions and two CNIH2 proteins in the A'/C' positions. The final LBD-TMD map from the A3A2A3A2 subtype was refined to a resolution of 7.7 Å (C2 symmetry), and displayed discontinuous transmembrane helices densities for the receptor and weak auxiliary protein densities. This lack of resolution is likely limited by the number of particles from the A3A2A3A2 subtype. Resolutions reported in Supplementary Table 1 are global estimated by gold standard FSC 0.143 criteria and local resolution estimations were calculated using ResMap[47]. Because the only resolvable arrangement of auxiliary proteins from all of the

AMPAR subtypes appeared to be the same, we employed an additional strategy aimed at improving resolution of the LBD-TMD layer, as described below.

The stack of 1,844,956 particles from Strategy #2 was first extracted to a box size of 548 × 548 pixels and then downsampled to 400 × 400 pixels. A consensus refinement was generated from these particles using homogenous refinement, followed by non-uniform refinement in cryoSPARC[49]. Using this map, a mask was generated around the ATD layer, including all possible locations for the three antibodies. This mask was used to subtract the ATD layer and antibody features from the consensus refinement, using signal subtraction in cryoSPARC[47]. This new dataset containing only the LBD-TMD layer underwent two iterations of reference-free 2D classification, resulting in 954,539 particles. This stack of 954,539 particles was separated into 10 classes using 3D heterogenous refinement without imposition of symmetry. One class consisting of 151,141 particles was selected for refinement, as it displayed density for continuous helices within the micelle, including density for TARP-γ8 at the B'/D' positions and CNIH2 at the A'/C' positions, equivalent to the stoichiometry observed in the LBD-TMD maps solved using focused classification (Supplementary Table 1). Refinement of this single class was performed in cryoSPARC consisting of a 4-step, iterative procedure described in Figure. S16. This procedure was iterated twice, resulting in a map at 3.45 Å resolution. To further improve the map, *ab initio* 3D classification was performed without symmetry imposed in order to remove 'junk' particles. One class showed clear features of the LBD-TMD layer, while the remaining classes were uninterpretable. The best class consisting of 132,427 particles was then subject to the 4-step refinement procedure described above, resulting in a 3.26 Å map by the gold-standard FSC (0.143).

The metadata and particle stack from the 3.26 Å map were then imported to RELION 3.0[48] for further classification. Particles were sorted using 3D classification without alignment (C1 symmetry, T=50, loose mask) in order to remove junk particles. Of the 8 classes, 6 of them displayed uninterpretable density (4%), one class showed clear secondary structure, but resolved only to ~8 Å resolution (8%), and the remaining class showed density for side-chains and improved density features for the helical-like density we surmise is SynDIG4 (88%). This class of 116,710 particles was re-imported to cryoSPARC for a final refinement that resulted in a final resolution of 3.25 Å (B-factor = 62.1) by the gold-standard FSC = 0.143. The EM density from this map, deemed the LBD-TMD$_{mix}$ map, was visualized in UCSF Chimera[50].

Model building

The ATD-Fab/scFv layers of the A1A2A1A2-S and A1A2A1A2-AS density maps were first rigid-body fit with structure of the ATD-Fab/scFv layers, including the carbohydrate groups, extracted from the A1A2A1A2 (PDB code: 6NJL), using UCSF Chimera[50], respectively. The resulting structures were manually adjusted in Coot[51], guided by well-resolved side chain densities and further refined by real-space refinement using Coot[51] and Phenix[52], yielding map to model cross correlation (cc) values for ATD-Fab/scFv layers of A1A2A1A2-S and A1A2A1A2-AS of 0.74 and 0.77, respectively.

For the LBD-TMD$_{A1/A2}$ map, we first rigid-body fit the recombinant di-heteromeric A1/A2-TARP-γ8 complex (PDB code: 6QKC) into the density. A homology model of CNIH2 was built using the CNIH3 subunit extracted from the homomeric GluA2-CNIH3 complex (PDB code: 6PEQ). This model was rigid-body fit to the map in Phenix[52]. Based on inspection of the density, we assigned TARP-γ8 and CNIH2 to the density in the B'/D' and A'/C' positions, respectively. Notably, flip/flop splicing sites and the R/G editing sites are interpretable in our maps and we assigned the flip/R and flop/R sequences for these two sites to GluA1 and GluA2, respectively, and built glutamine and arginine at the Q/R sites for the GluA1 and GluA2 subunits, respectively. Coordinates for MPQX were extracted from a previously solved GluA2 crystal structure (PDB code: 3KG2) and placed into the well-defined densities appropriately. Simplified molecular-input line-entry system (SMILES) string of JNJ-55511118 was imported to Coot[51] to generate the structure of JNJ-55511118, followed by manual fitting into the corresponding densities. Because prominent tube-shaped electron density surrounding the transmembrane domain of the receptor and the auxiliary proteins are likely from ordered lipid molecules, we fit these densities with alkane chains of complementary lengths. Notably, at the cytosolic boundary of the A'/C' positions, a single lipid molecule, denoted OCT906, bridges residues Val69 and Ser73 from TM2 with Ile573 from the M2 helix of GluA2. The resultant structure was manually adjusted in Coot[51], guided by well-defined side-chain densities from both the receptor and auxiliary protein densities. Subsequently, the structure was refined by real-space refinement in Coot[51] and by Phenix[52], placing restraints on clearly defined secondary structure elements and the appropriate NCS, yielding a map to model cc of 0.77. This structure was used as the initial model for building the LBD-TMD$_{mix}$ map. Comparisons of the LBD dimers between the LBD-TMD$_{A1/A2}$ and the GluA2-CNIH3 structures were done by superimposing the B/C LBD dimers and calculating the RMSD of the Cα atoms between these two dimers, and the change in the COM from the opposing A/D LBD dimers in PyMOL[62]. Comparisons of the TMD layers between the LBD-TMD$_{A1/A2}$ and the GluA2-CNIH3 structures were carried out by superimposing the two models, followed by calculations of the RMSD between the Cα atoms of the M1, M3, and M4 helices in PyMOL[62].

The LBD-TMD$_{A1/A2}$ model was used as a starting point to generate coordinates for the LBD-TMD$_{mix}$ model. Briefly, the LBD-TMD$_{A1/A2}$ model was first docked into the EM density of the LBD-TMD$_{mix}$ map by rigid-body fitting using Chimera[50]. Next, the auxiliary proteins were rigid-body fit independently into the EM density. Based on our structures, the appearance of only GluA2 subunits in the B/D positions allowed us to define occupancy of these positions by the GluA2 subunit. The A/C positions could be occupied by either GluA1, GluA3, or GluA4, therefore, non-conserved side-chains of these three subunits were modeled as alanines. The improved resolution of the LBD-TMD$_{mix}$ map permitted visualization of lipid densities and two prominent densities in the channel pore. Lipids were modeled as acyl chains unless resolution permitted modeling of lipid head groups. The densities inside the channel are unmodeled, but we speculate that the density near the apex of the selectivity filter could be a Na^+ ion. Ion-oxygen distances of ~2.6 Å from the carbonyl oxygen of R586 in the B-D positions are consistent with predicted distances of sodium binding sites, as well as MD simulations[53]. The density towards the bottom of the pore could either be a Na^+ ion or a water molecule, but is at insufficient resolution for speculation. The

C-terminal domains of AMPAR subunits and TARP-γ8 are unmodeled. Automatic real space refinement of the model was performed against one of the half-maps in Phenix with 2-fold symmetry imposed[52], with secondary structure and geometric restraints used to minimize over-fitting. Manual rebuilding in Coot was alternated with automated refinement in Phenix. For cross-validation, FSC curves were calculated between the refined model and the LBD-TMD_{mix} half-map used for refinement. Regions that lacked sufficient resolution for accurate establishment of amino acids were modeled as polyalanines, such as the TM3-TM4 loop in CNIH2. Regions with weak or no density were not modeled and are indicated by dashed lines, which include the M1-M2 linker, the TM1-TM2 loop of CNIH2, and a significant portion of the TARP-γ8 extracellular region.

To generate the complete structures of the A1A2A1A2-S and A1A2A1A2-AS complexes, the refined models of the ATD-Fab/scFv-PS/AS and LBD-TMD were fit into their respective whole maps in Chimera[50] and manually adjusted in Coot[51]. All of the final models have good stereochemistry as evaluated by MolProbity score[54] (Supplementary Table 1). Figures were prepared using UCSF Chimera[50], UCSF ChimeraX[55] and PyMOL[56].

Patch clamp recording

The DNA sequences encoding C-terminal GFP-tagged full length rat GluA1 (flip, Q in the Q/R site) and C-terminal mCherry-tagged full length rat TARP-γ8 were cloned into a bicistronic BacMam vector for baculovirus transduction. Whole cell recording was carried out on HEK293S GnTI (−) cells 18–24 hours after transduction with virus generated from the bicistronic GluA1-TARP-γ8 construct. To minimize cell death, 30 μM NBQX (2,3-Dioxo-6-nitro-1,2,3,4-tetrahydrobenzo[f]quinoxaline-7-sulfonamide, Tocris) was added 5–6 hrs post-infection. Pipettes were pulled to 2–4 MΩ resistance and were filled with an internal solution containing (in mM): 75 CsCl, 75 CsF, 5 EGTA and 10 HEPES, pH 7.3. The external solution contained (in mM): 160 NaCl, 2.4 KCl, 4 CaCl2, 4 MgCl2 and 10 HEPES, pH 7.3. Membrane voltage was held at −60 mV. The Axopatch 200B amplifier was used for data acquisition and pClamp 10 software was used for trace analysis. 10 mM glutamate was chosen as a saturating concentration for the peak responses. As the receptor complex with TARP-γ8 confers a slow augmentation of steady-state current during application of glutamate, to reach a plateau of the steady state current, we repeatedly applied glutamate for 1 s a total of 10 times at an interval of 2 s. Only the steady-state current of the last application was used for data analysis. A concentration of 10 μM JNJ-555511118 was applied before and during glutamate application for 1 s to measure the inhibition of glutamate-induced currents. Individual cells were only used once for recording; no repeated measurements were taken from the same cell.

Single molecule pulldown

Coverslips and glass slides were extensively cleaned, passivated, and coated with methoxy polyethylene glycol (mPEG) and 2% biotinylated PEG[57]. A flow chamber was created by drilling 0.75 mm holes in the quartz slide and by placing double-sided tape between the holes. A coverslip was placed on top of the slide and the edges were sealed with epoxy, creating small flow chambers. A concentration of 0.25 mg/mL streptavidin was then applied to the slide, allowed to incubate for 5 minutes, and washed off with T50 BSA buffer

consisting of 50 mM Tris, 50 mM NaCl and 0.25 mg/mL BSA, pH 8.0. Biotinylated anti-GluA2 15F1 mAb at 10 μg/mL was applied to the slide, allowed to incubate for 10 minutes, and washed off with 30 μL buffer A (20 mM Tris, pH 8.0, 150 mM NaCl, 0.075% (w/v) digitonin, 2 μM MPQX and 2 μM JNJ-55511118) supplemented with 0.2 mg/mL BSA. Mouse brain supernatant, prepared as previously described under "isolation of native hippocampal AMPA receptors", was either diluted 1:600 to visualize GluA1, GluA3, TARP-γ8, and SynDIG4 containing complexes, or 1:100 to visualize the less abundant complexes with the GluA4 subunit. Supernatant was applied to the chamber, incubated for 5 minutes, and washed off with 30 μL of buffer A. Detection antibodies were generated by labeling subunit- or auxiliary protein-specific antibodies with NHS ester Alexa Fluor dyes. The labeling efficiency of all detection mAbs was at least 1 dye per mAb, as judged by comparison of the dye and antibody concentration after removal of unreacted dye. Fluorophore-labeled detection mAbs were applied to the chamber for 5 minutes at a concentration of 1 to 3 μg/mL, washed off with 30 μL of buffer A, and the chamber was immediately imaged using a Leica DMi8 TIRF microscope with an oil-immersion 100x objective. Images were captured using a back-illuminated EMCCD camera (Andor iXon Ultra 888) with a 133 × 133 μm imaging area and a 13 μm pixel size. This 13 μm pixel size corresponds to 130 nm on the sample due to the 100x objective. For counting GluA1, GluA3 and GluA4 subunits, mean spot count per image and standard deviation were calculated from 90 total images collected from three separate chambers. The total number of complexes was calculated by adding the number of GluA1, GluA3, and GluA4 spots, and subtracting the number of colocalized GluA1 and GluA3 spots. Each SiMPull experiment included a negative control in a separate chamber wherein the anti-GluA2 capture antibody was not applied but the other steps remained identical. The observed spot count from this chamber was used to estimate background fluorescence. The results of each SiMPull experiment are averaged across at least three independent samples from experiments conducted on at least two different days.

For single-molecule colocalization, two images were acquired in the same region of interest and the position of each molecule was calculated using a custom python script. Molecules located within a 4-pixel radius were considered to be colocalized. At least 12 images were averaged for each experiment. The colocalization of GluA4 with other subunits and auxiliary proteins was not calculated because of the low abundance of GluA4-containing receptors. To visualize complexes harboring the GluA4 subunit, it was necessary to apply a high concentration of mouse brain supernatant, resulting in such a high spot density for other complexes so as to render counting individual complexes not possible.

Photobleaching movies were acquired by exposing the imaging area for 160 seconds. To count the number of TARP-γ8 subunits, single-molecule fluorescence time traces of GFP-tagged anti-TARP-γ8 Fab were generated using a custom python script. Each trace was manually scored as having one to four bleaching steps or was discarded if no clean bleaching steps could be identified. This distribution of bleaching steps fits a binomial distribution for a dimeric protein based on an estimated GFP maturation of 80%. A total of 600 molecules were evaluated from three separate movies. Scoring was verified by assessing the intensity of the spot; on average, the molecules that bleach in 2 steps were twice as bright as those that bleach in 1 step.

Western blot analysis

Purified hippocampal AMPARs were loaded onto SDS-PAGE gels and transferred to a nitrocellulose membrane. Antibodies used for detection were anti-GluA1 (Millipore #04–823, 1:1000), anti-GluA2 (Thermo Fisher #PA5–19496, 1:1000), anti-GluA3 (Invitrogen #32–0400, 1:1000), anti-GluA4 (Millipore #ab1508, 1:1000), anti-PSD95 (Abcam #ab-18258, 1:1000), and anti-TARP-γ8 + anti-CNIH2 (mAbs generated in our lab, see methods, 1:1000). IRDye 800 CW anti-mouse/rabbit secondary antibodies were used for visualization. Blots were developed by adding secondary antibodies at a ratio of 1:10,000.

Data availability statement

The cryo-EM maps and coordinates for overall, ATD layer and LBD-TMD layer of the A1A2A1A2-symmetric (S) and A1A2A1A2-asymmetric (AS) complexes have been deposited in the Electron Microscopy Data Bank (EMDB) under accession numbers EMD-23283 and EMD-23284 and in the Protein Data Bank (PDB) under accession codes 7LDD and 7LDE, respectively. The cryo-EM maps for overall, ATD layer and LBD-TMD layer of A1A2A3A2-AS1, A1A2A3A2-AS2, A3A2A3A2-S and A3A2A3A2-AS complexes have been deposited in the EMDB under accession numbers EMD-23285, EMD-23286, EMD-23287 and EMD-23288, respectively. The cryo-EM maps of A1A2A3A2-AS3 and A1A2AXA2 have been deposited in the EMDB under accession numbers EMD-23289 and EMD-23290, respectively. The cryo-EM map and coordinates for the LBD-TMD_{mix} complex has been deposited in the EMDB and PDB under accession codes EMD-23292 and 7LEP, respectively.

Animal use statement

200 Adult (6–8 weeks) C57BL/6 mice (both male and female) were ordered from Charles River Laboratories for hippocampal dissection. Prior experiments allowed us to determine the minimum number of mice sufficient for our study. No randomization, blinding, or experimental manipulations were performed on these animals. All mice were euthanized under proper Institutional Animal Care and Use Committee (IACUC) protocols, consistent with the recommendations of the Panel on Euthanasia of the American Veterinary Medical Association (AVMA) and carried out only by members of Dr. Gouaux's lab approved on the IACUC protocol TR01_IP00000905.

Cell lines statement

Sf9 cells for expression of Baculovirus are from Thermofisher (12659017, lot 421973). HEK293S GnTI^{-} cells (Ric15) for protein expression and electrophysiology studies are from Reeves P, et al.[58]. They were not authenticated experimentally for these studies and tested negative for Mycoplasma contamination.

Extended Data

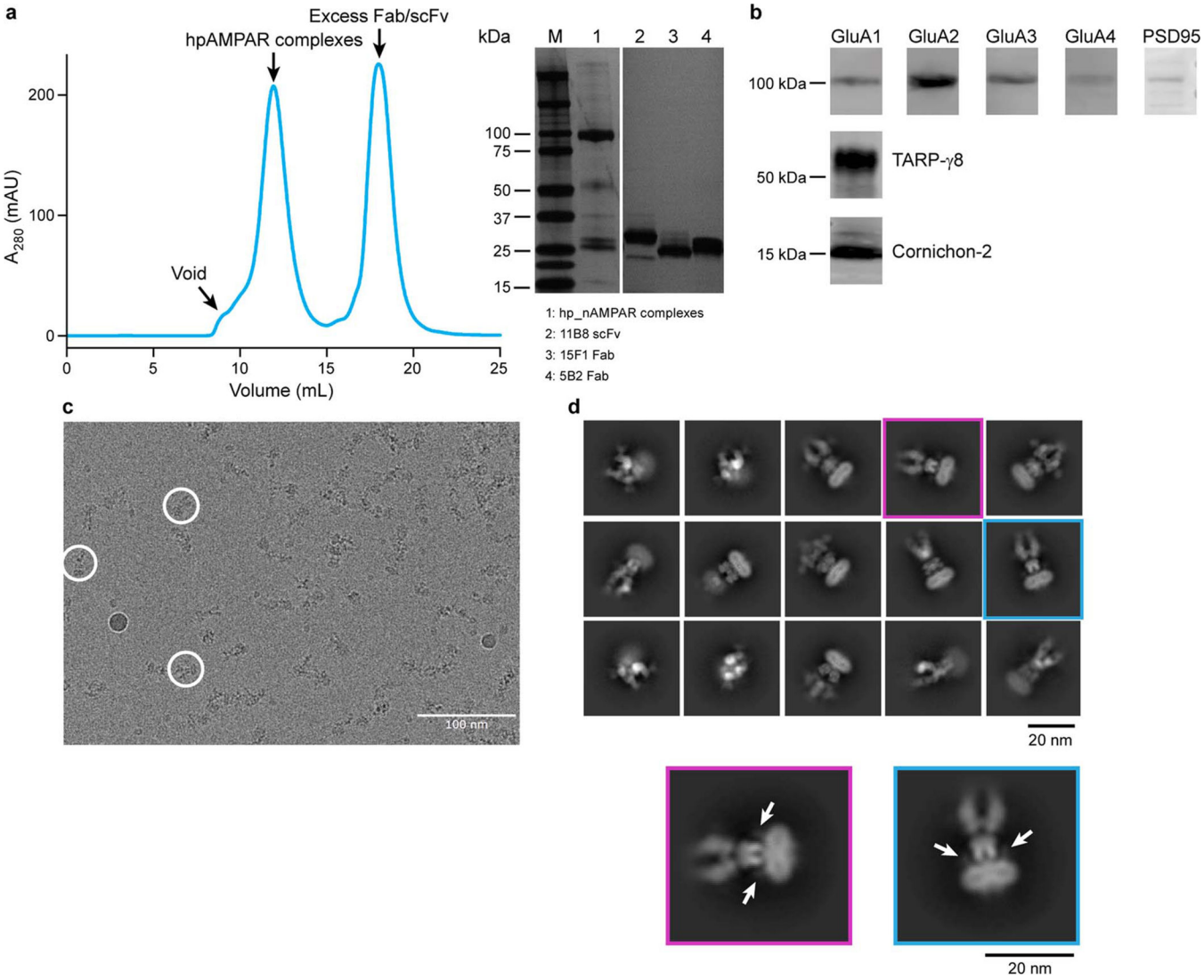

Extended Data Figure 1. Biochemical characterization and cryo-EM analysis of hp AMPAR complexes.

a. Representative SEC profile of hippocampal AMPAR complexes. Inset shows an SDS-PAGE gel of AMPAR complexes and antibody fragments used for cryo-EM grid preparation, visualized by silver staining. The gel was repeated three times from different batches of purification with similar results.

b. Western blot analysis of isolated AMPAR complexes using antibodies against GluA1, GluA2, GluA3, GluA4, PSD95, TARP-γ8 and Cornichon-2. The uncropped blot can be found in Supplementary Fig. 1 and blotting was repeated three times with similar results.

c. A representative cryo-EM micrograph of hpAMPAR complexes. The experiments were repeated four times with similar results.

d. Selected 2D class averages. Protrusions extending out of the detergent micelle are indicated by arrows, corresponding to the extracellular domain of TARP-γ8. Similar results were obtained from four repeated experiments.

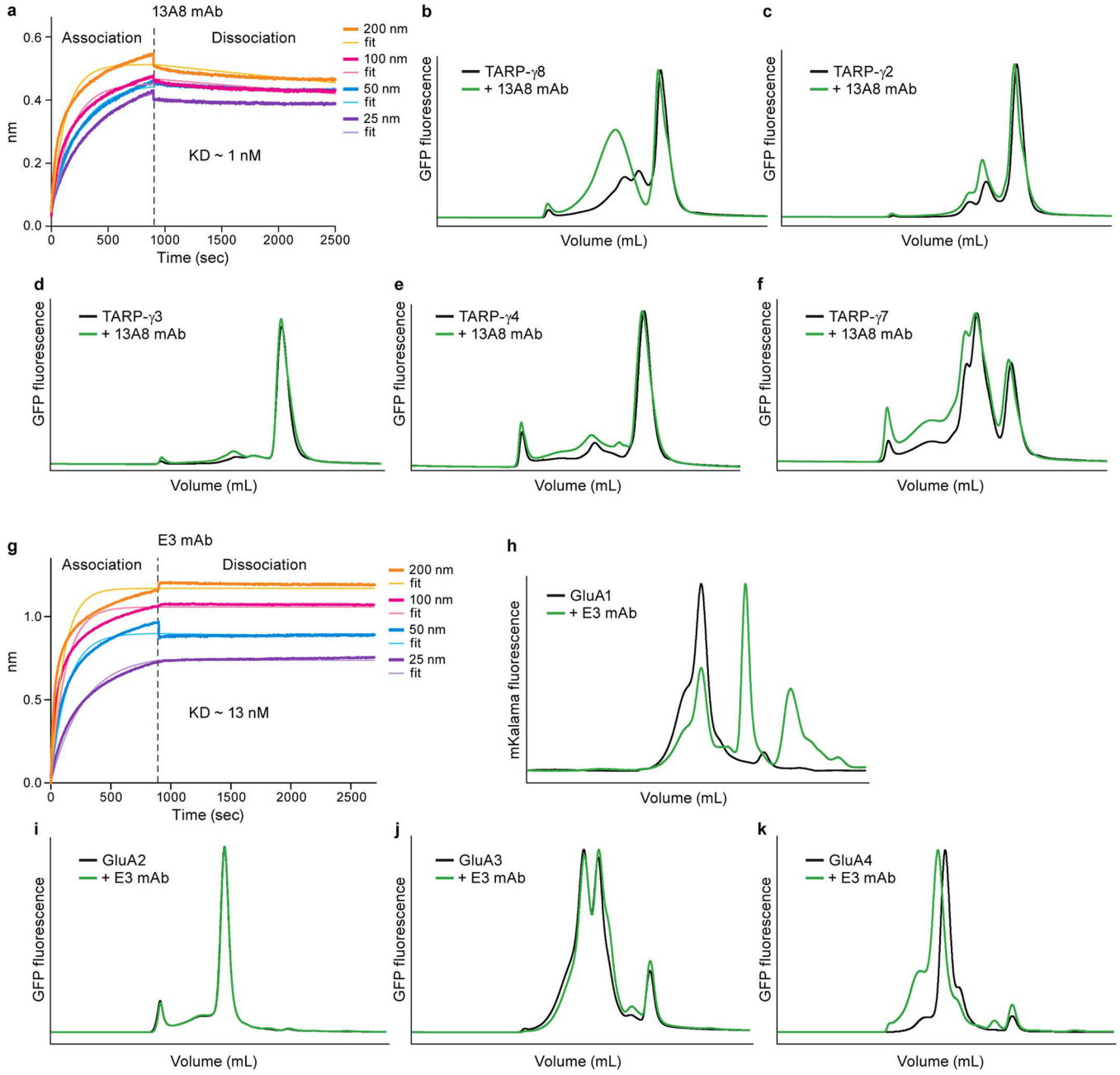

Extended Data Figure 2. Characterization of monoclonal antibodies 13A8 and E3

a. Octet measurements of the 13A8 mAb binding to TARP-γ8. Concentrations of the 13A8 mAb ranging from 25–200 nM were applied.

b-f. FSEC profiles of recombinant GFP-tagged TARP-γ8 (**b**), TARP-γ2 (**c**), TARP-γ3 (**d**), TARP-γ4 (**e**) and TARP-γ7 (**f**) with 13A8 mAb (green traces) and without 13A8 mAb (black traces), detecting GFP fluorescence. Only the TARP-γ8 trace is shifted by the 13A8 mAb.

g. Octet measurements of the E3 mAb binding to GluA4.

h-k. FSEC profiles of recombinant mKalama-tagged GluA1 (**h**), GFP-tagged GluA2 (**i**), GFP-tagged GluA3 (**j**) and GFP-tagged GluA4 (**k**) with E3 mAb (green traces) and without

E3 mAb (black traces), detecting mKalama/GFP fluorescence. Only GluA4 receptors are shifted by the E3 mAb.

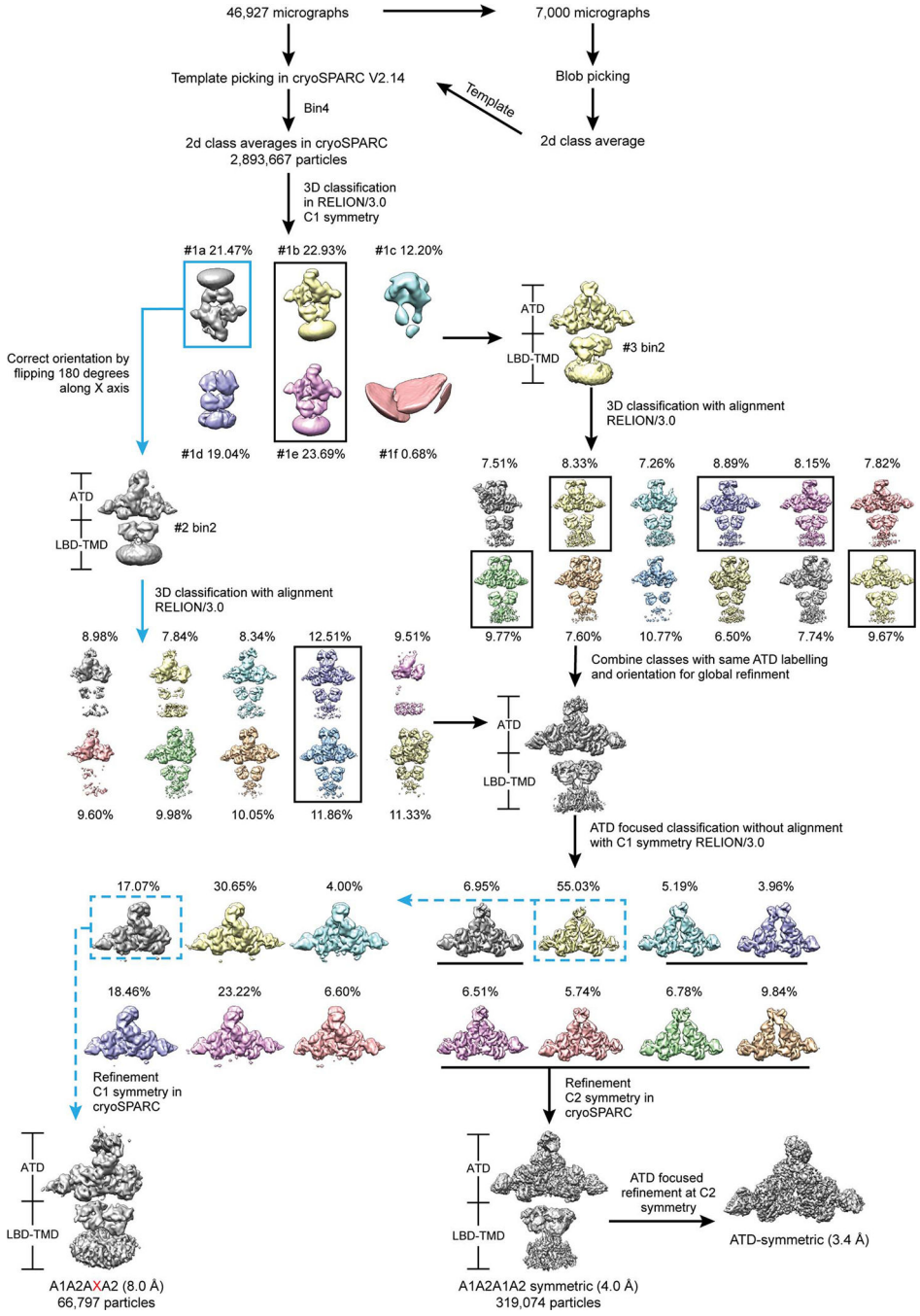

Extended Data Figure 3. A representative flow chart of data processing focused on the whole receptor and ATD layer using image processing strategy #1.

A total of 2,893,667 particles were picked from 46,927 motion-corrected micrographs in cryoSPARC v2.14. Classes showing clear receptor features were kept after several rounds of 2D classification, resulting in retention of 2,893,667 particles. Next, 3D classification with a large sampling degree was performed to further remove junk classes in RELION 3.0.

Another around of 3D classification was carried out to sort receptors with the same Fab/scFv combination. Classes with the same ATD labeling and orientation were combined and subjected to ATD focused classification without alignment. For the A1A2A1A2-symmetric subtype, the ATD layer was classified into eight classes, of which one class occupying the largest population (55%) had the least well-resolved secondary structure features. Another round of ATD focused classification was performed on this class, producing a subtype with one unlabeled subunit, denoted as A1A2AXA2. Three remaining classes showing the most well-defined secondary structure features were selected for final refinement with C2 symmetry, producing a map at a resolution of 4 Å. ATD-focused refinement with C2 symmetry was carried out to improve map density in the ATD, yielding an ATD-A1A2A1A2-symmetric map at a resolution of 3.4 Å.

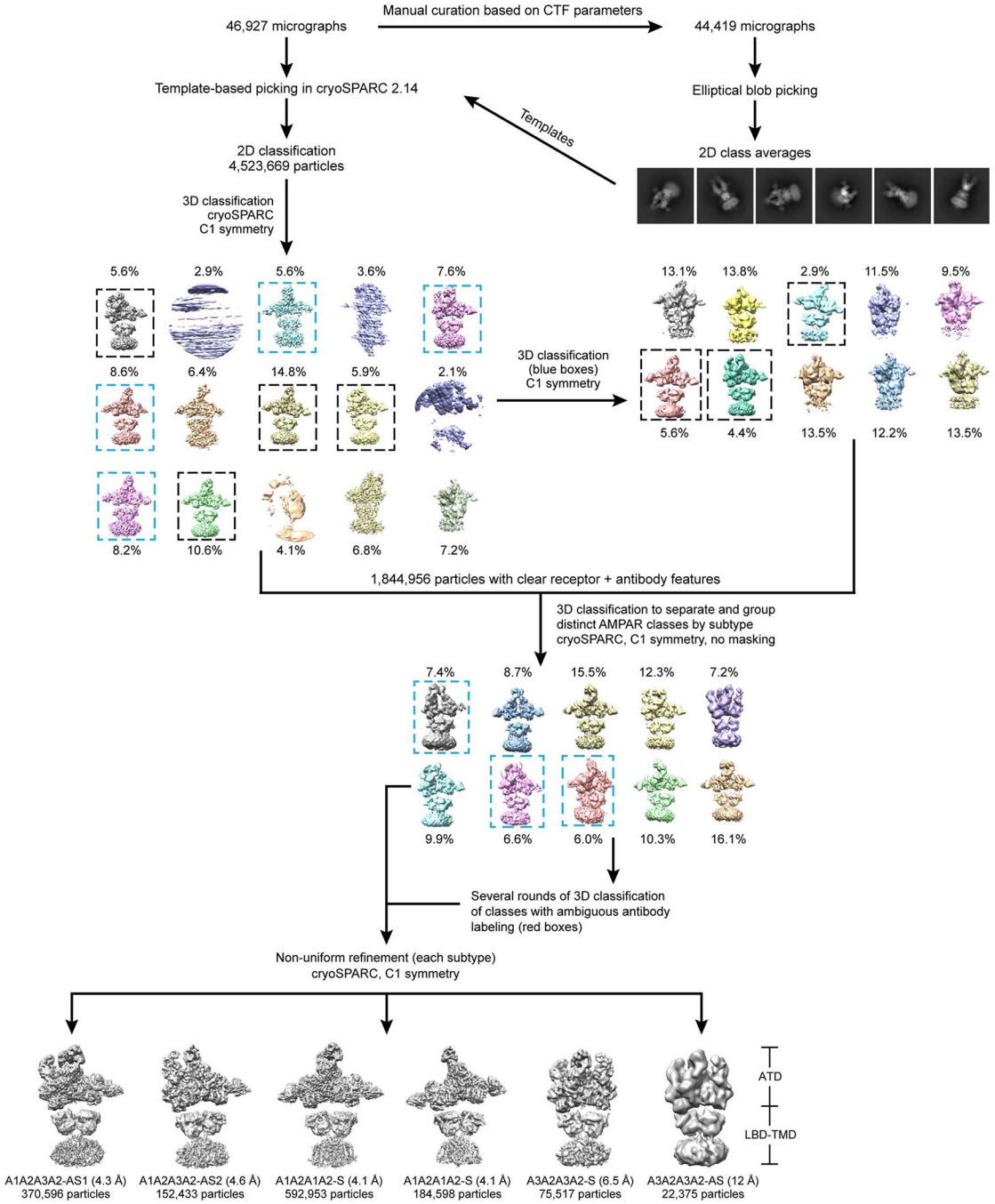

Extended Data Figure 4. Data processing workflow to determine AMPAR subtypes using image processing strategy #2.

Motion-corrected micrographs were first curated based on ice thickness, motion correction, CTF fit and astigmatism. Template-based picking was used to autopick 6,002,517 particles in cryoSPARC v2.14. To remove junk particles and false positives, multiple rounds of 2D and 3D classification were performed, selecting only classes that showed discernible receptor features, resulting in a particle stack of 1,844,956 particles. To sort receptors based on subtype (AMPAR subunit stoichiometry and tilting), multiple rounds of 3D classification were performed without symmetry imposed or masking. Particles from classes showing

clear labeling with antibodies were grouped into distinct subtypes. Each of the AMPAR subtypes were refined separately. This strategy elucidated three different heteromeric AMPAR subtypes comprised of both symmetric and asymmetric conformations.

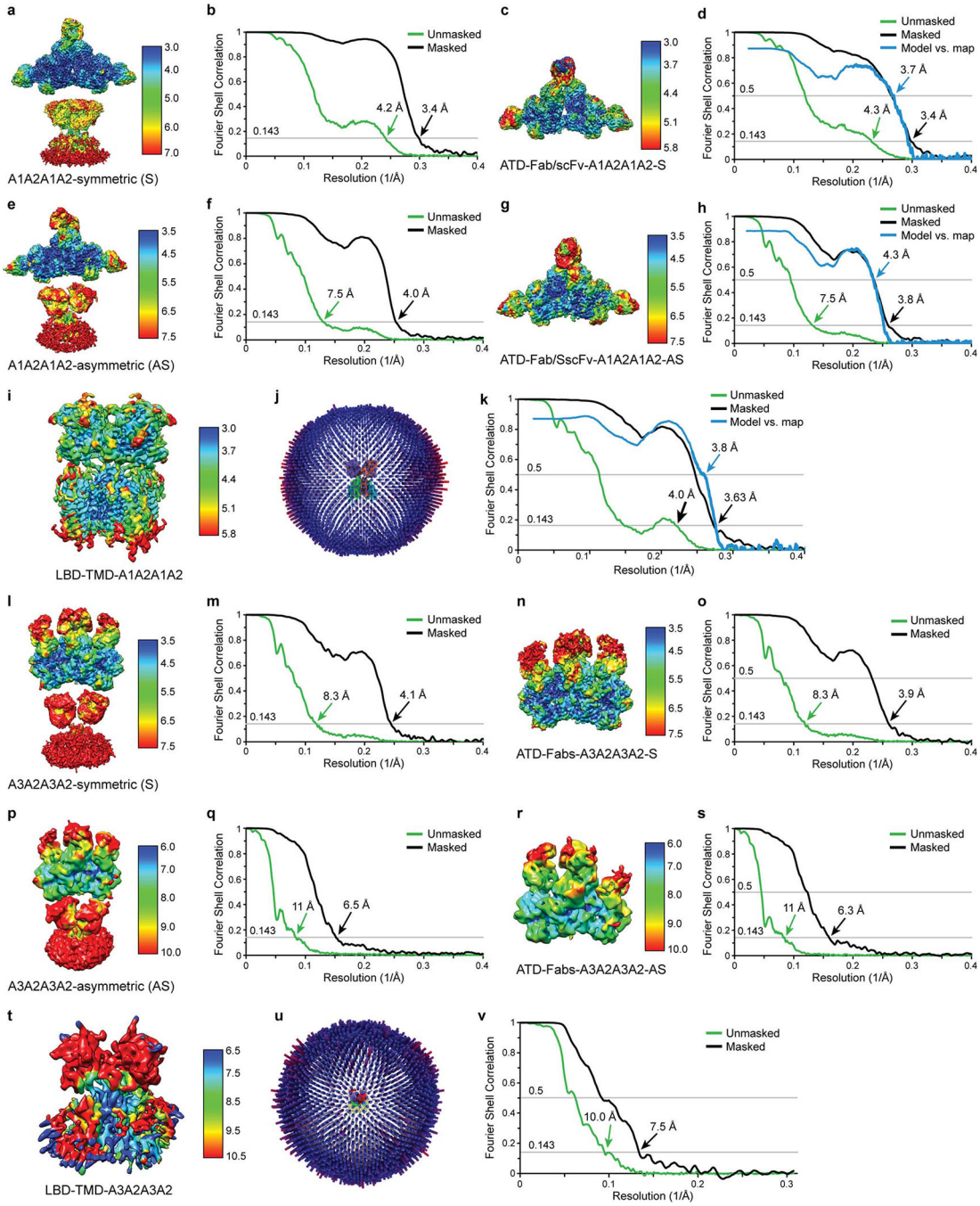

Extended Data Figure 5. 3D reconstructions of dimeric-GluA1/A2 and dimeric-GluA2/A3 complexes.

a, c, e, g, i. Local resolution estimates of the entire GluA1/A2-symmetric map (**a**), ATD-layer of the GluA1/A2-symmetric map (**c**), entire GluA1/A2-asymmetric map (**e**), the ATD-layer of GluA1/A2-asymmetric map (**g**) and the LBD-TMD layers of the GluA1/A2 map (**i**).

d, h, k. FSC curves before and after masking and between the model and the final maps of ATD-layer of the GluA1/A2-symmetric (**d**), ATD-layer of the GluA1/A2-asymmetric (**h**) and LBD-TMD layers of GluA1/A2 (**k**).

j. Angular distribution of the LBD-TMD layers of the GluA1/A2 map.

l, n, p, r, t. Local resolution estimates of the entire GluA2/A3-symmetric map (**l**), ATD-layer of the GluA2/A3-symmetric map (**n**), entire GluA2/A3-asymmetric map (**p**), ATD-layers of the GluA2/A3-asymmetric map (**r**) and LBD-TMD layers of the GluA2/A3 map (**t**).

b, f, m, o, q, s, v. FSC curves before and after masking maps of whole GluA1/A2-symmetric (**b**), entire GluA1/A2-asymmetric (**f**), entire GluA2/A3-symmetric (**m**), ATD-layer of GluA2/A3-symmetric (**o**), entire GluA2/A3-asymmetric (**q**), ATD-layer of the GluA2/A3-asymmetric (**s**) and the LBD-TMD layers of GluA2/A3 (**v**).

u. Angular distribution of the LBD-TMD layers of the GluA2/A3 map.

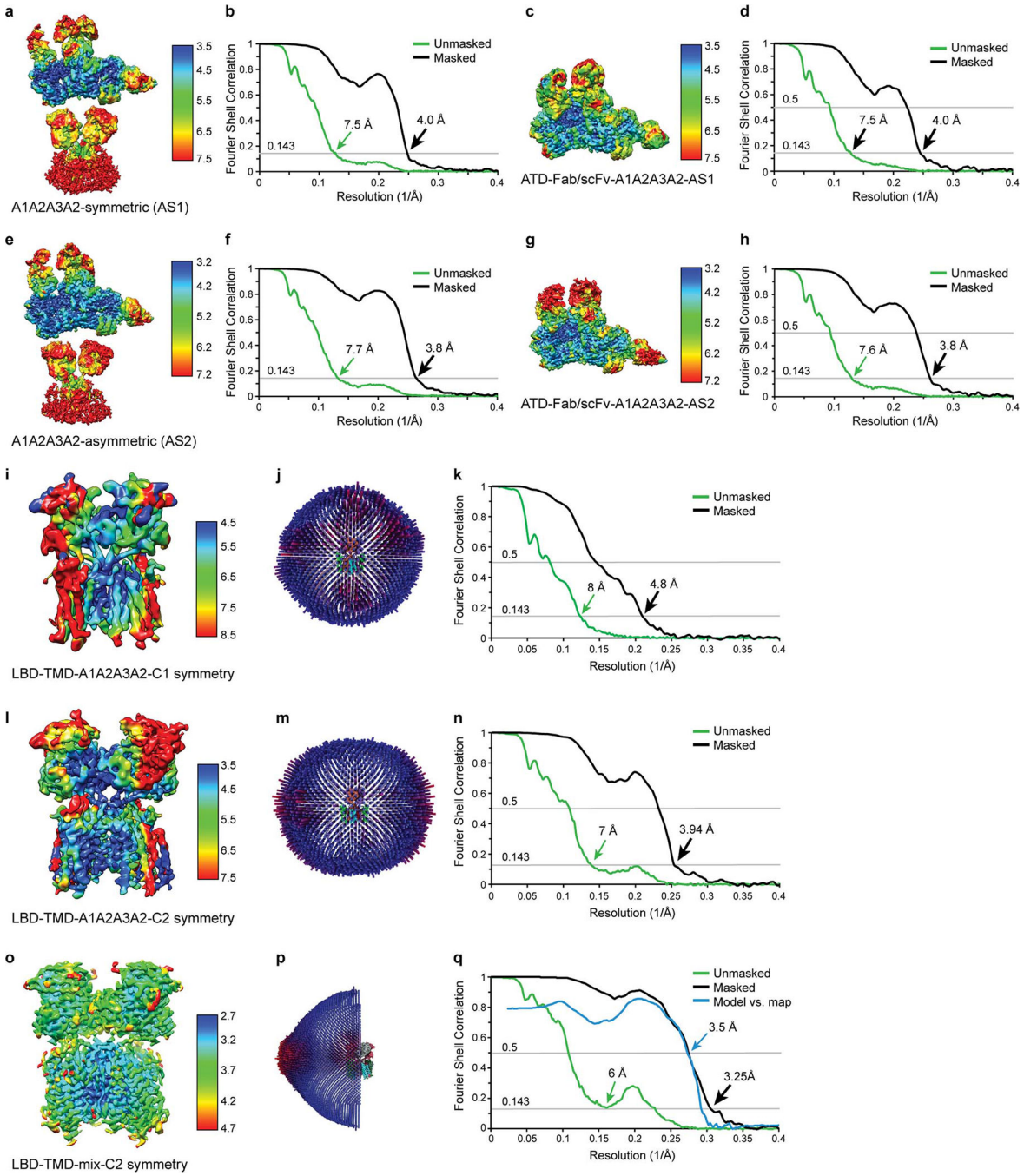

Extended Data Figure 6. 3D reconstructions of trimeric-GluA1/A2/A3 complexes and the LBD-TMD$_{mix}$ map.

a, c, e, g, i, l, o. Local resolution estimates of the entire GluA1/A2/A3-asymmetric 1 map (**a**), ATD-layer of the GluA1/A2/A3-asymmetric 1 map (**c**), entire GluA1/A2/A3-asymmetric 2 map (**e**), ATD-layer of the GluA1/A2/A3-asymmetric 2 map (**g**), LBD-TMD layers of GluA1/A2/A3 without symmetry (**i**), LBD-TMD layers of GluA1/A2/A3 with C2 symmetry imposed (**l**), and LBD-TMD$_{mix}$ map (**o**).

b, d, f, h, k, n. FSC curves before and after masking maps of the entire GluA1/A2/A3-asymmetric 1 receptor (**b**), the ATD-layer of GluA1/A2/A3-asymmetric 1 (**d**), entire GluA1/A2/A3-asymmetric 1 (**f**), ATD-layer of the GluA1/A2/A3-asymmetric 2 (**h**), LBD-TMD layers of GluA1/A2/A3 without symmetry (**k**) and with C2 symmetry (**n**).
j, m, p. Angular distribution of LBD-TMD layers of GluA1/A2/A3 maps with C1 symmetry (**j**) or C2 symmetry (**m**), and the LBD-TMD_{mix} map (**p**).
q. FSC curves before and after masking and between the model and the final maps of the LBD-TMD_{mix} map.

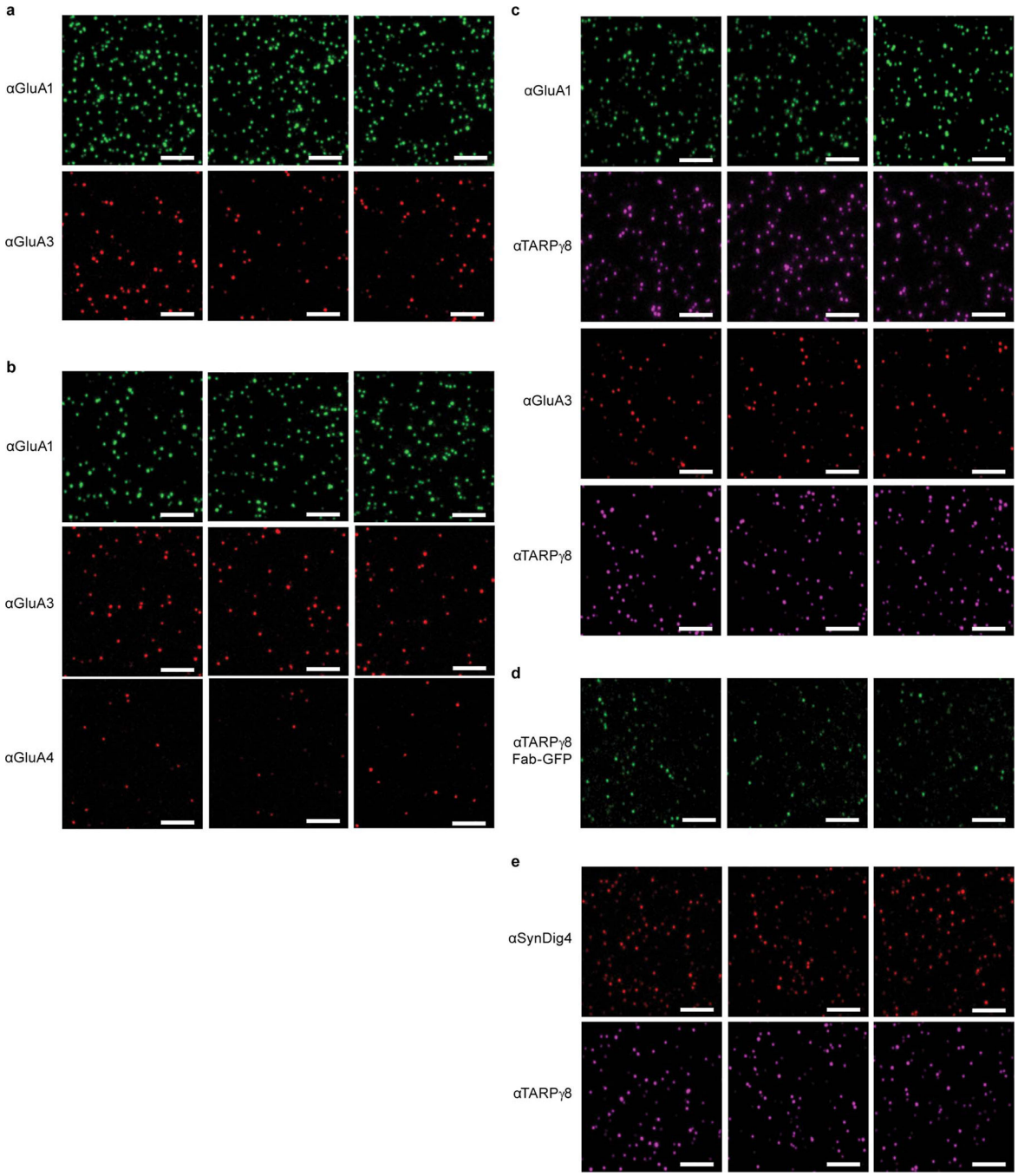

Extended Data Figure 7. Representative TIRF images for native AMPA receptor complexes captured with 15F1 mAb.

Fluorescence detection with (**a**) anti-GluA1-Alexa488 mAb (αGluA1) and anti-GluA3-Alexa594 mAb (αGluA3), (**b**) anti-GluA1-Alexa488 mAb, anti-GluA3-Alexa594 mAb, and anti-GluA4-Alexa594 mAb (αGluA4), (**c**) anti-GluA1-Alexa488 mAb, anti-GluA3-Alexa594 mAb, and anti-TARP-γ8 mAb (for each colocalization experiment), (**d**) anti-TARP-γ8 Fab-GFP (αTARP-γ8), and (**e**) anti-SynDIG4-Alexa594 mAb (αSynDIG4) and anti-TARP-γ8-Alexa647 mAb. Scale bar in each image represents 5 μm.

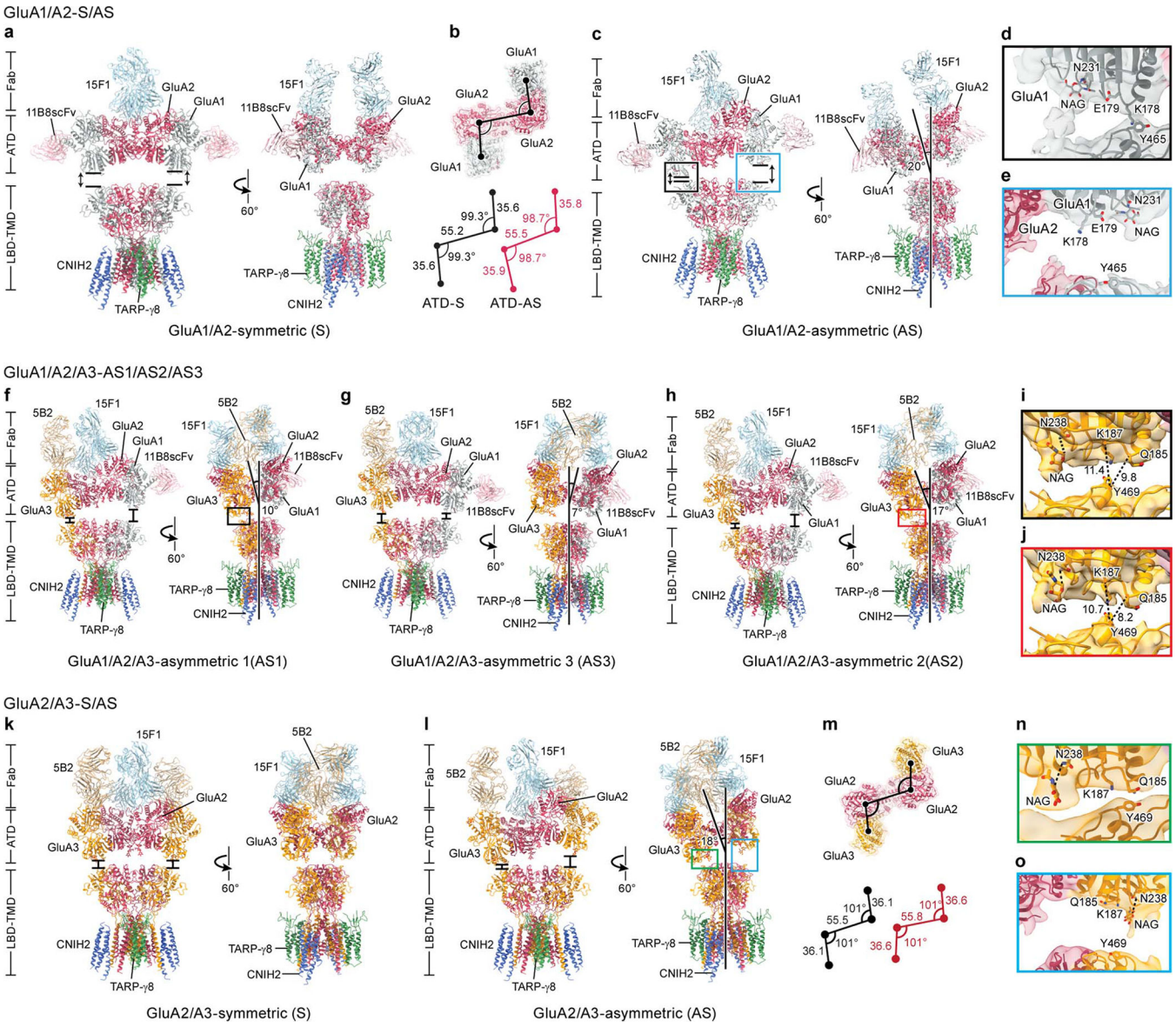

Extended Data Figure 8. Structures of the dimeric GluA1/A2 receptor, trimeric GluA1/A2/A3 receptor and dimeric GluA2/A3 receptor complexes in symmetric and asymmetric conformations.

a, c. Cryo-EM structures of the GluA1/A2 subtype in symmetric (**a**) and asymmetric (**c**) conformations viewed parallel to the membrane. GluA1, GluA2, TARP-γ8, and CNIH2 are grey, red, green and blue, respectively. Antibody fragments 11B8 scFv and 15F1 Fab are pink and cyan, respectively.

b. ATD layer analysis of symmetric and asymmetric conformations. ATD model of symmetric state is shown in upper panel, in which center of masses (COMs) of each subunit are indicated by black circles. The lower two panels show the distances (in Ångstrom) and angles determined by COMs of symmetric (left) and asymmetric (right) conformations.

d-e. Close contacts between the ATD layer and LBD layer in the asymmetric conformations. Close-up views of the ‘left’ side (**d**) and ‘right’ side (**e**) of the ATD-LBD interfaces as indicated in the black and cyan rectangles.

f-h. Cryo-EM structures of the trimeric GluA1/A2/A3 subtype in asymmetric conformations with different tilted angles and orientations viewed parallel to the membrane. GluA1, GluA2, GluA3, TARP-γ8 and CNIH2 are colored in grey, red, orange, green and blue, respectively. Antibody fragments 11B8 scFv, 15F1 Fab, 5B2 Fab are in pink, cyan and light yellow colors, respectively.

i-j. Zoomed-in views of ATD-LBD interfaces in the asymmetric states (**f** and **h**) as indicated in the black and red rectangles. The distances are defined by the Cα atoms of indicated residues.

k, l. Cryo-EM structures of the dimeric GluA2/A3 subtype in symmetric (**k**) and asymmetric (**l**) conformations viewed parallel to the membrane.

m. ATD layer analysis of the symmetric and asymmetric conformations. An ATD model of the symmetric state is shown in the upper panel. The COMs of each subunit are in black circles. The lower two panels show the distances (in Ångstrom) and angles determined by COMs of symmetric (left) and asymmetric (right) conformations.

n-o. Close contacts between the ATD layer and LBD layer in the asymmetric conformations. Zoomed-in views of left side (**n**) and right side (**o**) of the ATD-LBD interfaces as indicated in the green and cyan rectangles.

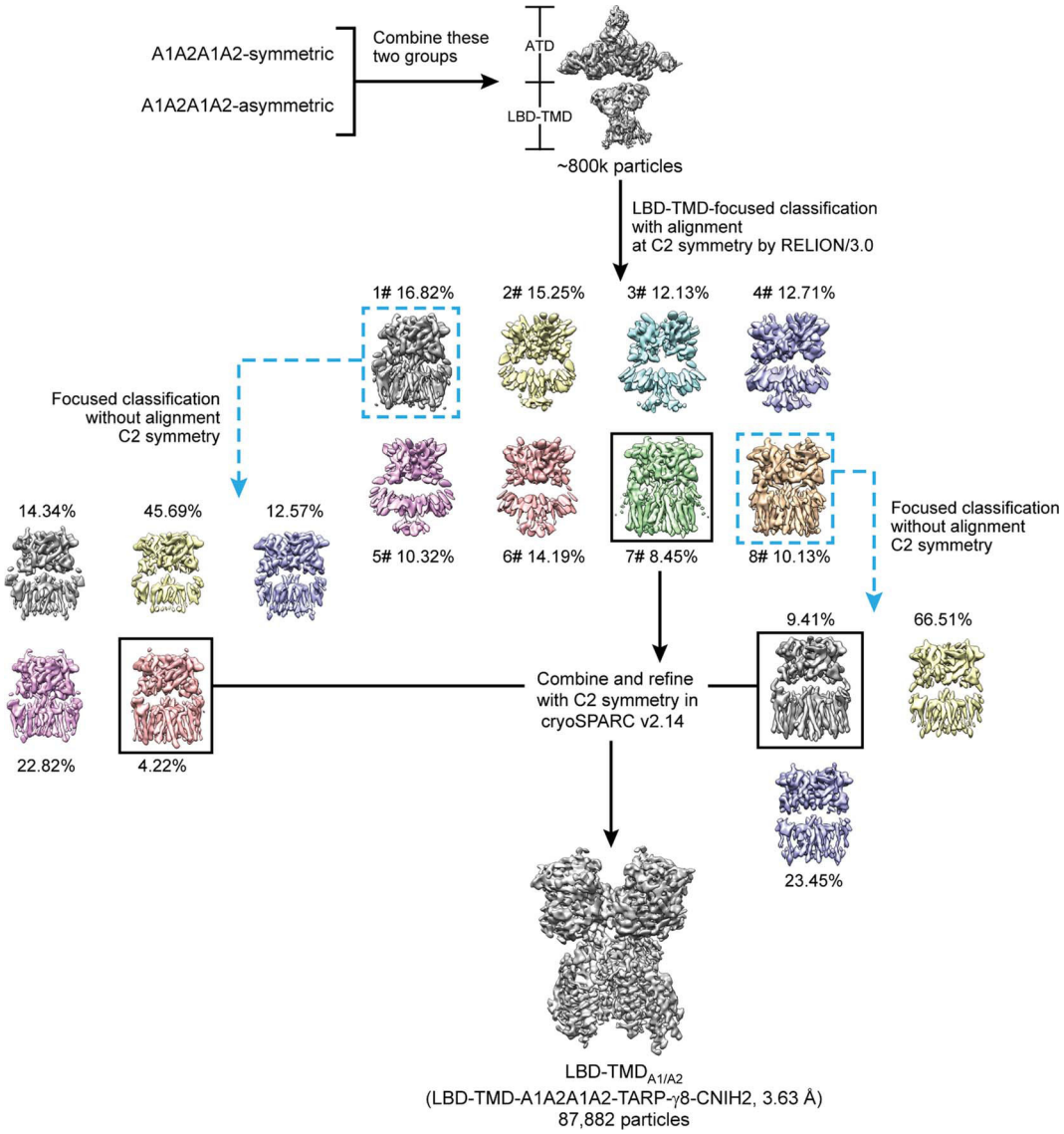

Extended Data Figure 9. Flow chart of data processing for hippocampal AMPAR complexes focused on the LBD-TMD layers.

Particles corresponding to both the symmetric and asymmetric A1A2A1A2 subtype were combined and subjected to LBD-TMD focused 3D classification with alignment in RELION 3.0, resulting in three good classes with continuous transmembrane helical densities. Another round of classification without alignment was carried out for classes 1 and 8. Classes displaying strong density for TMD and auxiliary proteins were combined for refinement in cryoSPARC v2.14, yielding the LBD-TMD$_{A1/A2}$ map at a resolution of 3.63 Å.

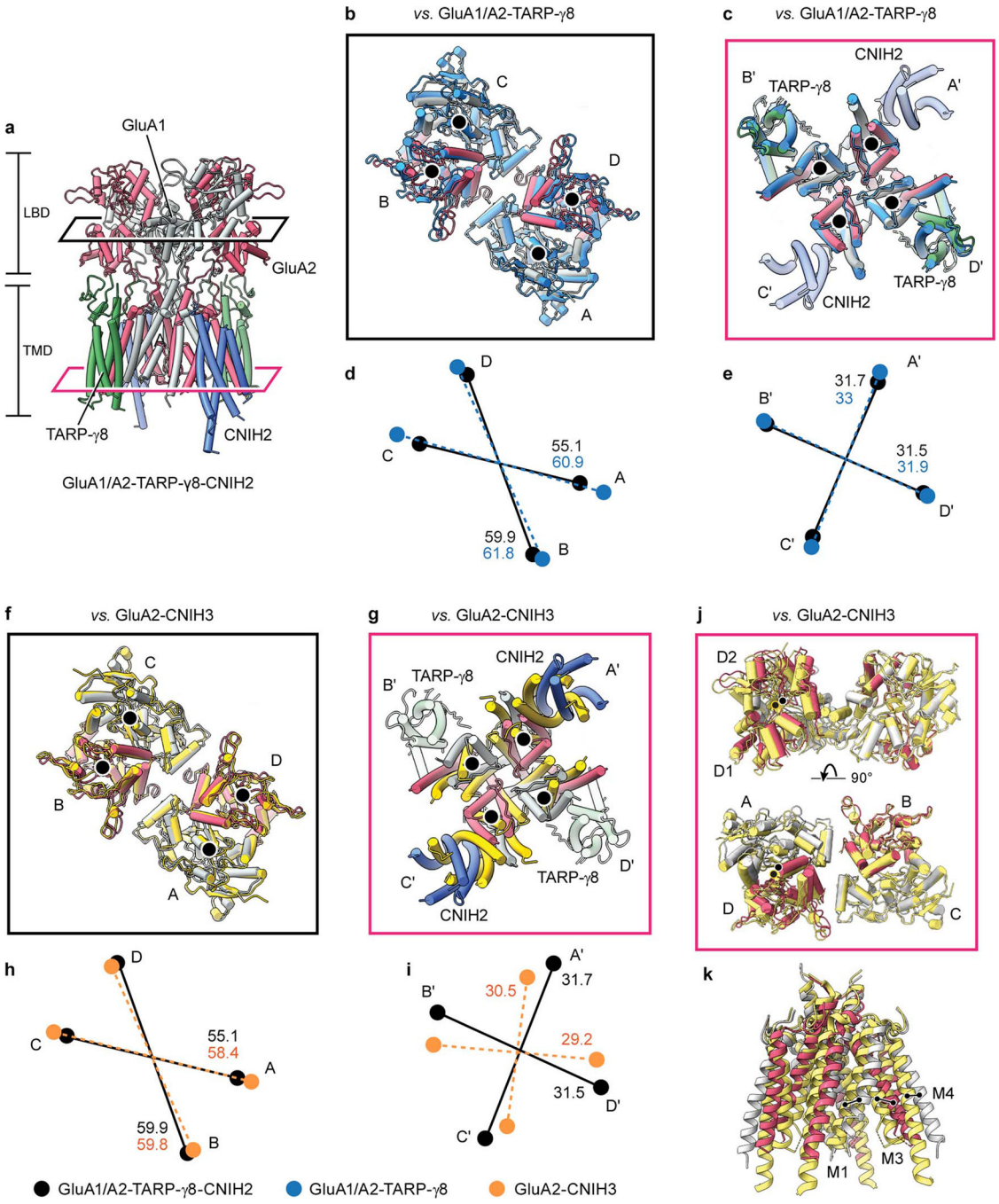

Extended Data Figure 10. Conformational differences in the LBD and TMD layers between native and recombinant AMPAR-auxiliary protein complexes.

a. Reference model and orientation of the hippocampal GluA1/A2-TARP-γ8-CNIH2 complex. GluA1, GluA2, TARP-γ8, and CNIH2 are in grey, red, green, and blue, respectively.

b-e. Superposition of hippocampal GluA1/A2-TARP-γ8-CNIH2 with recombinant GluA1/A2-TARP-γ8 complexes (PDB code: 6qkc) to show the differences in the LBD (**b, d**) and TMD (**c, e**) layers. Recombinant GluA1/A2-TARP-γ8 is in blue. COMs of LBD and

TMD layers of each subunit are shown in colored circles. The schematic diagrams illustrate the subunit arrangement differences in distance (Ångstrom) of the LBD (**d**) and TMD (**e**) layers of these two complexes.

f-i. Superposition of the hippocampal GluA1/A2-TARP-γ8-CNIH2 structure with the recombinant GluA2-CNIH3 complex (PDB code: 6peq) to show the differences in the LBD (**f, h**) and TMD (**g, i**) layers. Recombinant GluA2-CNIH3 is in yellow. COMs of LBD and TMD layers of each subunit are shown in colored circles. The schematic diagrams illustrate the subunit arrangement differences in distance (Ångstrom) of the LBD (**h**) and TMD (**i**) layers of these two complexes.

j. The B/C LBD dimers from the hippocampal GluA1/A2-TARP-γ8-CNIH2 structure and the GluA2-CNIH3 complex (PDB code: 6peq) were superimposed, exhibiting a 3.2 Å shift in the COM (black circles) between the opposing A/D LBD dimers.

k. Superposition of the M1, M3, and M4 helices of the hippocampal GluA1/A2-TARP-γ8-CNIH2 structure with the recombinant GluA2-CNIH3 complex (PDB code: 6peq), highlighting the rotation and compression of the GluA2-CNIH3 TMD layer. Equivalent positions of the Cα atoms from the M1 (V538), M3 (I600), and M4 (L805) helices of the GluA2-CNIH3 structure are shifted by 4.5 Å, 5.7 Å, and 4.7 Å, respectively.

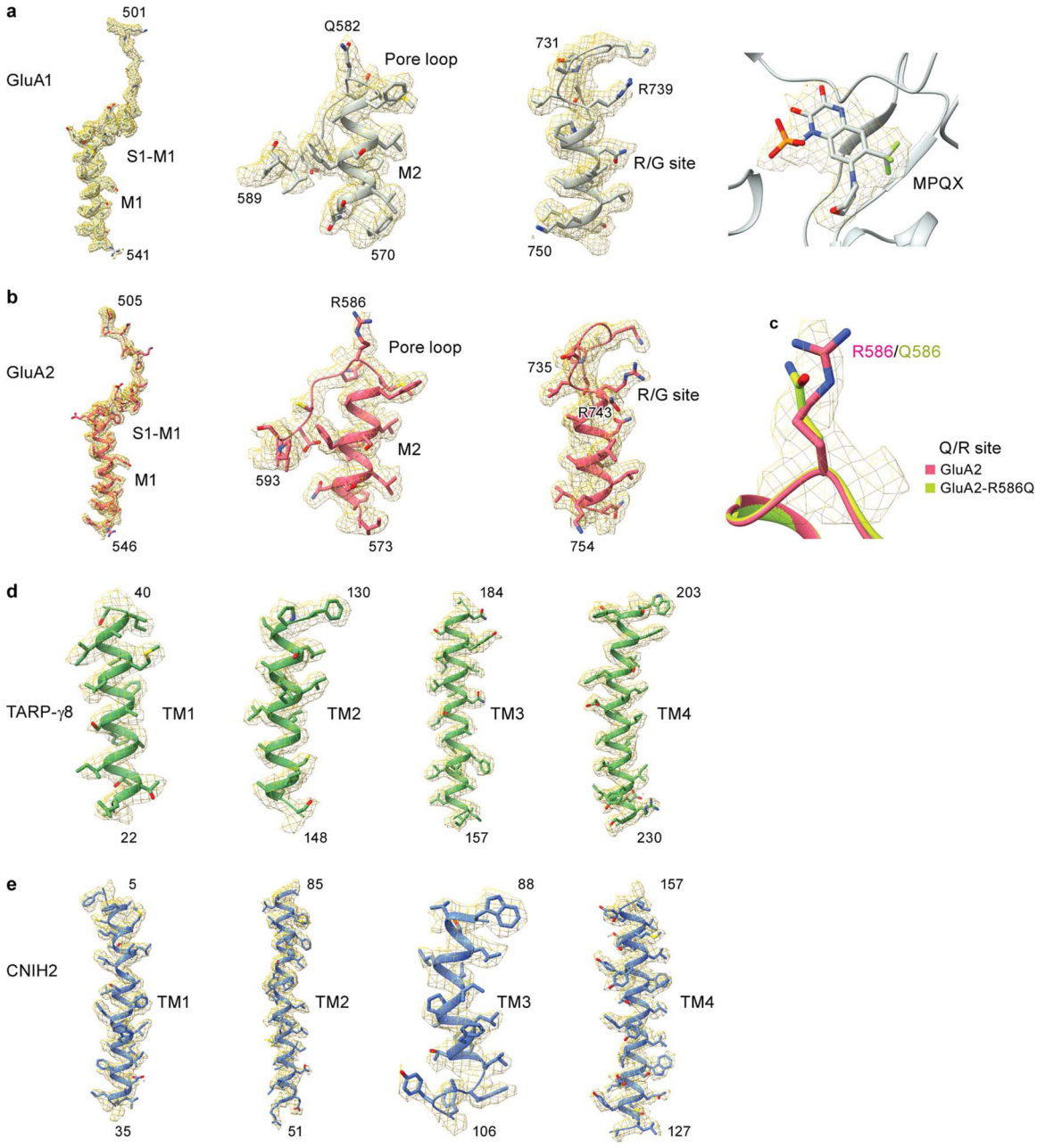

Extended Data Figure 11. Representative densities of the LBD-TMD$_{A1/A2}$ or LBD-TMD$_{mix}$ complexes maps.

a. The S1-M1, M2-pore loop, R/G site, and MPQX from GluA1 are isolated from LBD-TMD$_{A1/A2}$, contoured at 0.085.

b. S1-M1, M2-pore loop, and R/G site from GluA2 are isolated from LBD-TMD$_{A1/A2}$, contoured at 0.085.

c. Comparison of the differences by fit Arg and Gln into the GluA2 Q/R site density.

d. Four transmembrane helices (TM1-TM4) in TARP-γ8 are isolated from LBD-TMD$_{mix}$, contoured at 0.15.

e. Four transmembrane helices (TM1-TM4) in CNIH2 are isolated from LBD-TMD_{mix}, contoured at 0.13.

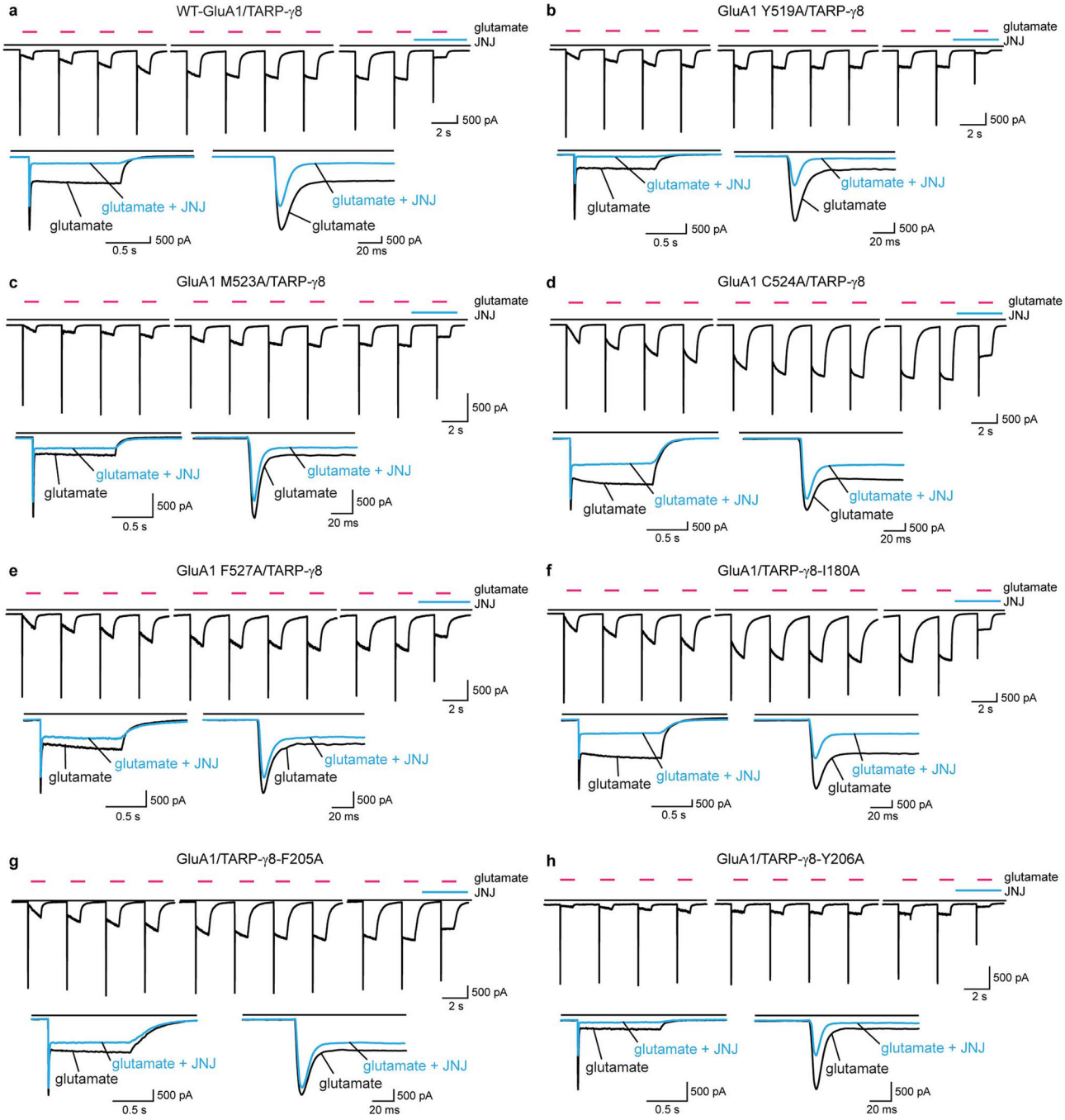

Extended Data Figure 12. Electrophysiological recordings of GluA1-TARP-γ8 mutants.

a. Current responses of wild-type GluA1-TARP-γ8 complexes evoked by repeated application of 10 mM glutamate with 10 pulses, each for a duration time of 1s to reach a plateau of the steady-state current. 10 μM JNJ-555511118 was applied before and during glutamate application for 1 s to measure the inhibition of glutamate-induced currents. The

lower two insets illustrate the inhibition effect of JNJ-55511118 on the steady-state current by overlaying currents without (the last application) and with JNJ-55511118 at time scale of 500 ms (left) and 20 ms (right).

b-h. Representative recordings for the mutations derived from GluA1 (**b-e**) and TARP-γ8 (**f-h**) with the same recording condition as wild-type.

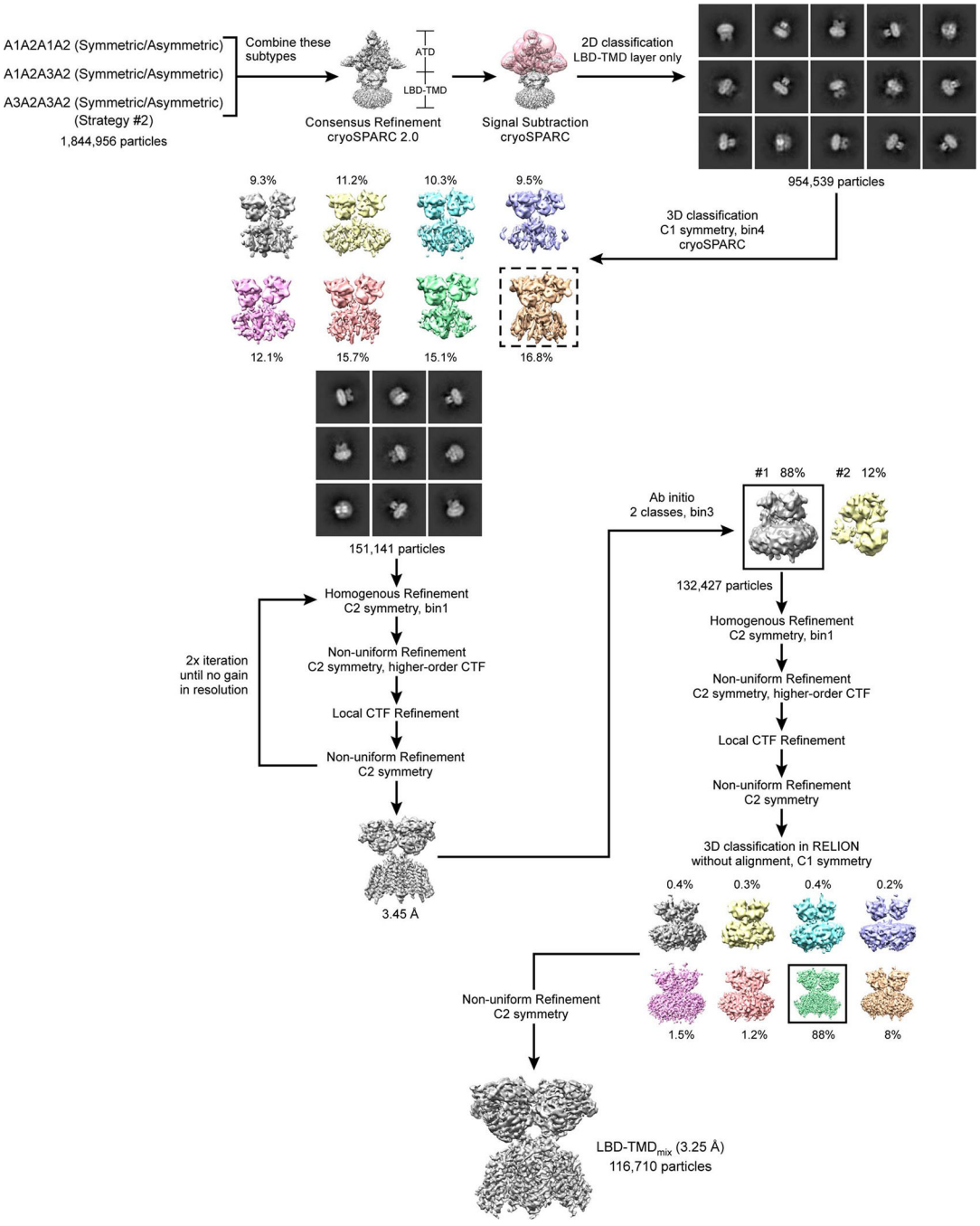

Extended Data Figure 13. LBD-TMD$_{mix}$ image processing strategy #2

Particles post 2D/3D classification cleanup from strategy #2 were combined into a single stack and refined, and unless otherwise specified, all subsequent processing was performed in cryoSPARC v2.14. Signal subtraction was implemented using the consensus refinement and a soft mask created around the ATD layer and all possible binding sites of the antibodies. Several rounds of 2D classification were used to remove false positives and particles still harboring the ATD layer. This cleaned stack of particles underwent 3D classification (C1 symmetry) resulting in a single class displaying continuous transmembrane density features. Particles from this class were subject to 2D classification to remove a small subset of junk particles. An iterative, sequential, refinement procedure consisting of 1) Homogenous refinement, 2) Non-uniform Refinement, 3) Local CTF Refinement and 4) Non-uniform Refinement, was used to improve the resolution of the stack of 151,141 particles. This procedure was iterated 2x until no resolution improvement was obtained, resulting in a 3.45 Å map. Particles from this map were then subjected to Ab Initio classification permitting removal of junk particles. A new stack of 132,427 particles was then subjected to the previously described 4-step refinement procedure for one iteration, before 3D classification was performed in RELION 3.0 to remove junk particles. This final particle stack was subjected to Non-uniform Refinement in cryoSPARC to obtain the LBD-TMD_{mix} map at 3.25 Å.

Supplementary Material

Refer to Web version on PubMed Central for supplementary material.

Acknowledgements

We thank the Pacific Northwest Cryo-EM Center (PNCC) and OHSU MMC for microscope use, D. Cawley, P. Streeter, Y. Zhong and N. Sheldon for generating antibodies, A. Goehring for mouse dissections, Mark Mayer for his guidance and advice on electrophysiology experiments, J. Elferich for help writing SiMPull processing scripts, S. Chen for the help initiating the project, L. Vaskalis for assistance with figures, F. Jalali-Yazdi and H. Owen forhelp with manuscript preparation and R. Nicoll and Gouaux laboratory members for helpful discussions. PNCC is supported by NIH grant U24GM129547 and accessed through EMSL (grid.436923.9), a DOE Office of Science User Facility sponsored by the Office of Biological and Environmental Research. T.H. and J.M. were supported by the NIGMS grant R35GM122569. This work was supported by the NINDS grant R01NS038631 to E.G. T.H. and E.G. are investigators of the Howard Hughes Medical Institute. The content is solely the responsibility of the authors and does not necessarily represent the official views of National Institutes of Health.

References

1. Diering GH & Huganir RL The AMPA receptor code of synaptic plasticity. Neuron 100, 314–329 (2018). [PubMed: 30359599]
2. Jackson AC & Nicoll RA The expanding social network of ionotropic glutamate receptors: TARPs and other transmembrane auxiliary subunits. Neuron 70, 178–199 (2011). [PubMed: 21521608]
3. Collingridge GL, Kehl SJ & McLennan H Excitatory amino acids in synaptic transmission in the Schaffer collateral-commissural pathway of the rat hippocampus. J Physiol 334, 33–46 (1983). [PubMed: 6306230]
4. Bliss TV & Lomo T Long-lasting potentiation of synaptic transmission in the dentate area of the anaesthetized rabbit following stimulation of the perforant path. J Physiol 232, 331–356 (1973). [PubMed: 4727084]
5. Rosenmund C, Stern-Bach Y & Stevens CF The tetrameric structure of a glutamate receptor channel. Science 280, 1596–1599, (1998). [PubMed: 9616121]
6. Sobolevsky AI, Rosconi MP, & Gouaux E X-ray structure, symmetry and mechanism of an AMPA-subtype glutamate receptor. Nature 462, 745–756, (2009). [PubMed: 19946266]

7. Traynelis SF et al. Glutamate receptor ion channels: structure, regulation, and function. Pharmacol Rev 62, 405–496, (2010). [PubMed: 20716669]
8. Keinanen K et al. A family of AMPA-selective glutamate receptors. Science. 249, 556–560, (1990). [PubMed: 2166337]
9. Schwenk J et al. Regional diversity and developmental dynamics of the AMPA-receptor proteome in the mammalian brain. Neuron 84, 41–54 (2014). [PubMed: 25242221]
10. Wenthold RJ, Petralia RS, Blahos JI & Niedzielski AS Evidence for multiple AMPA receptor complexes in hippocampal CA1/CA2 neurons. J. Neurosci. 16, 1982–1989 (1996). [PubMed: 8604042]
11. Kamalova A & Nakagawa T AMPA receptor structure and auxiliary subunits. J Physiol (2020).
12. Tomita S et al. Functional studies and distribution define a family of transmembrane AMPA receptor regulatory proteins. J Cell Biol 161, 805–816 (2003). [PubMed: 12771129]
13. Schwenk J et al. Functional proteomics identify cornichon proteins as auxiliary subunits of AMPA receptors. Science 323, 1313–1319 (2009). [PubMed: 19265014]
14. Chen L et al. Stargazin regulates synaptic targeting of AMPA receptors by two distinct mechanisms. Nature 408, 936–943 (2000). [PubMed: 11140673]
15. Herguedas B et al. Architecture of the heteromeric GluA1/2 AMPA receptor in complex with the auxiliary subunit TARP gamma8. Science 364 (2019).
16. Nakagawa T Structures of the AMPA receptor in complex with its auxiliary subunit cornichon. Science 366, 1259–1263 (2019). [PubMed: 31806817]
17. Jain A et al. Probing cellular protein complexes using single-molecule pull-down. Nature 473, 484–488 (2011). [PubMed: 21614075]
18. Zhao Y, Chen S, Swensen AC, Qian WJ & Gouaux E Architecture and subunit arrangement of native AMPA receptors elucidated by cryo-EM. Science 364, 355–362 (2019). [PubMed: 30975770]
19. Maher MP et al. Discovery and characterization of AMPA receptor modulators selective for TARP-gamma8. J Pharmacol Exp Ther 357, 394–414 (2016). [PubMed: 26989142]
20. Lu W et al. Subunit composition of synaptic AMPA receptors revealed by a single-cell genetic approach. Neuron 62, 254–268 (2009). [PubMed: 19409270]
21. Jacobi E & von Engelhardt J Diversity in AMPA receptor complexes in the brain. Curr Opin Neurobiol 45, 32–38 (2017). [PubMed: 28376410]
22. Morise J et al. Distinct cell surface expression patterns of N-Glycosylation site mutants of AMPA-type glutamate receptor under the homo-oligomeric expression conditions. Int J Mol Sci 21 (2020).
23. Fukaya M et al. Abundant distribution of TARP gamma-8 in synaptic and extrasynaptic surface of hippocampal neurons and its major role in AMPA receptor expression on spines and dendrites. Eur J Neurosci 24, 2177–2190 (2006). [PubMed: 17074043]
24. Rouach N et al. TARP gamma-8 controls hippocampal AMPA receptor number, distribution and synaptic plasticity. Nat Neurosci 8, 1525–1533 (2005). [PubMed: 16222232]
25. Kato AS et al. Hippocampal AMPA receptor gating controlled by both TARP and cornichon proteins. Neuron 68, 1082–1096 (2010). [PubMed: 21172611]
26. Carrillo E et al. Mechanism of modulation of AMPA receptors by TARP-gamma8. J Gen Physiol 152 (2020).
27. Plested AJ & Mayer ML AMPA receptor ligand binding domain mobility revealed by functional cross linking. J. Neurosci. 29, 11912–11923 (2009). [PubMed: 19776277]
28. Baranovic J et al. Dynamics of the ligand binding domain layer during AMPA receptor activation. Biophys J 110, 896–911 (2016). [PubMed: 26910426]
29. Harmel N et al. AMPA receptors commandeer an ancient cargo exporter for use as an auxiliary subunit for signaling. PLoS One 7, e30681 (2012). [PubMed: 22292017]
30. Boudkkazi S, Brechet A, Schwenk J & Fakler B Cornichon2 dictates the time course of excitatory transmission at individual hippocampal synapses. Neuron 82, 848–858 (2014). [PubMed: 24853943]

31. Gill MB, Kato AS, Wang H & Bredt DS AMPA receptor modulation by cornichon-2 dictated by transmembrane AMPA receptor regulatory protein isoform. Eur J Neurosci 35, 182–194 (2012). [PubMed: 22211840]
32. Herring BE et al. Cornichon proteins determine the subunit composition of synaptic AMPA receptors. Neuron 77, 1083–1096 (2013). [PubMed: 23522044]
33. Sommer B, Kohler M, Sprengel R & Seeburg PH RNA editing in brain controls a determinant of ion flow in glutamate-gated channels. Cell 67, 11–19, doi:10.1016/0092-8674(91)90568-j (1991). [PubMed: 1717158]
34. Burnashev N, Villarroel A & Sakmann B Dimensions and ion selectivity of recombinant AMPA and kainate receptor channels and their dependence on Q/R site residues. J. Physiology 496.1, 165–173 (1996).
35. Swanson GT, Kamboj SK & Cull-Candy SG Single-channel properties of recombinant AMPA receptors depend on RNA editing, splice variation, and subunit composition. J. Neurosci. 17, 58–69 (1997). [PubMed: 8987736]
36. Bowie D & Mayer ML Inward rectification of both AMPA and kainate subtype glutamate receptors generated by polyamine-mediated ion channel block. Neuron 15, 453–462 (1995). [PubMed: 7646897]
37. Lomeli H et al. Control of kinetic properties of AMPA receptor channels by nuclear RNA editing. Science 266, 1709–1713, doi:10.1126/science.7992055 (1994). [PubMed: 7992055]
38. Kirk LM et al. Distribution of the SynDIG4/proline-rich transmembrane protein 1 in rat brain. J Comp Neurol 524, 2266–2280 (2016). [PubMed: 26660156]
39. Matt L et al. SynDIG4/Prrt1 is required for excitatory synapse development and plasticity underlying cognitive function. Cell Rep 22, 2246–2253 (2018). [PubMed: 29490264]
40. Troyano-Rodriguez E, Mann S, Ullah R & Ahmad M PRRT1 regulates basal and plasticity-induced AMPA receptor trafficking. Mol Cell Neurosci 98, 155–163 (2019). [PubMed: 31216424]
41. Penn AC et al. Hippocampal LTP and contextual learning require surface diffusion of AMPA receptors. Nature 549, 384–388 (2017). [PubMed: 28902836]
42. Goehring A et al. Screening and large-scale expression of membrane proteins in mammalian cells for structural studies. Nat Protoc 9, 2574–2585 (2014). [PubMed: 25299155]
43. Coleman JA, Green EM & Gouaux E X-ray structures and mechanism of the human serotonin transporter. Nature 532, 334–339 (2016). [PubMed: 27049939]
44. Kawate T & Gouaux E Fluorescence-detection size-exclusion chromatography for precrystallization screening of integral membrane proteins. Structure 14, 673–681 (2006). [PubMed: 16615909]
45. Sultan FA Dissection of different areas from mouse hippocampus. Bio Protoc 3 (2013).
46. Mastronarde DN Automated electron microscope tomography using robust prediction of specimen movements. J Struct Biol 152, 36–51 (2005). [PubMed: 16182563]
47. Punjani A, Rubinstein JL, Fleet DJ & Brubaker MA cryoSPARC: algorithms for rapid unsupervised cryo-EM structure determination. Nat Methods 14, 290–296 (2017). [PubMed: 28165473]
48. Zivanov J et al. New tools for automated high-resolution cryo-EM structure determination in RELION-3. Elife 7 (2018).
49. Punjani A, Zhang H & Fleet DJ Non-uniform refinement: adaptive regularization improves single-particle cryo-EM reconstruction. Nat Methods 17, 1214–1221 (2020). [PubMed: 33257830]
50. Pettersen EF et al. UCSF Chimera--a visualization system for exploratory research and analysis. J Comput Chem 25, 1605–1612 (2004). [PubMed: 15264254]
51. Emsley P & Cowtan K Coot: model-building tools for molecular graphics. Acta Crystallogr D Biol Crystallogr 60, 2126–2132 (2004). [PubMed: 15572765]
52. Afonine PV et al. Real-space refinement in PHENIX for cryo-EM and crystallography. Acta Crystallogr D Struct Biol 74, 531–544 (2018). [PubMed: 29872004]
53. Biedermann J, Braunbeck S, Plested AJ & Sun H Non-selective cation permeation in an AMPA-type glutamate receptor. bioRxiv (2020).

54. Chen VB et al. MolProbity: all-atom structure validation for macromolecular crystallography. Acta Crystallogr D Biol Crystallogr 66, 12–21 (2010). [PubMed: 20057044]

55. Goddard TD et al. UCSF ChimeraX: Meeting modern challenges in visualization and analysis. Protein Sci 27, 14–25 (2018). [PubMed: 28710774]

56. The PyMOL Molecular Graphics System (Schrodinger, LLC, 2020).

57. Jain A, Liu R, Xiang YK & Ha T Single-molecule pull-down for studying protein interactions. Nat Protoc 7, 445–452 (2012). [PubMed: 22322217]

58. Reeves PJ, Callewaert N, Contreras R & Khorana HG Structure and function in rhodopsin: high-level expression of rhodopsin with restricted and homogeneous N-glycosylation by a tetracycline-inducible N-acetylglucosaminyltransferase I-negative HEK293S stable mammalian cell line. Proc Natl Acad Sci U S A 99, 13419–13424 (2002). [PubMed: 12370423]

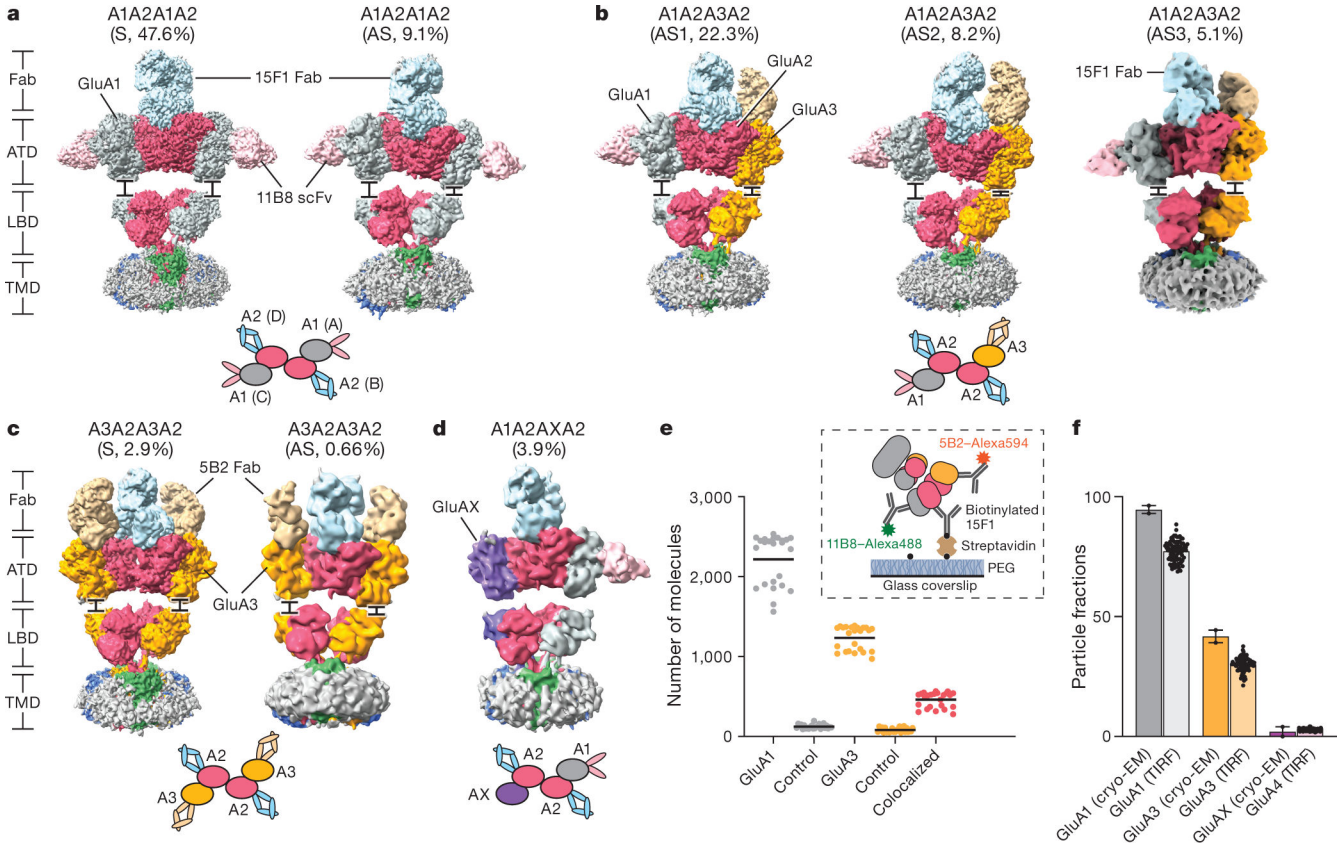

Figure 1. Cryo-EM and single molecule fluorescence analysis of hpAMPAR complexes.

a-d. Cryo-EM maps of the four resolved complexes, viewed parallel to the membrane. Symmetric and asymmetric conformations within one complex are indicated. GluA1, GluA2, GluA3, GluAX, where 'X' represents an unidentified subunit, and potential auxiliary proteins are grey, red, orange, purple and blue/green, respectively. The anti-GluA1 11B8 scFv, the anti-GluA2 15F1 Fab, and the anti-GluA3 5B2 Fab are pink, light blue, and light yellow, respectively. Insets are cartoons showing the subunit arrangement and antibody fragment labeling of the ATD layer.

e. The total number of GluA1, GluA3, and colocalized GluA1/GluA3 subunit-containing molecules detected by SiMPull are shown. See Methods for description of control experiments. We observed 37% colocalization of GluA3 spots with GluA1 spots. N=25 images examined over two independent experiments. The inset shows schematic depiction of AMPAR SiMPull.

f. Distribution of AMPAR subunits from cryo-EM and SiMPull experiments. The number of each subunit in the single particle cryo-EM dataset was counted based on the presence of an identifying scFv or Fab fragment. Particle fractions were averaged across two cryo-EM datasets obtained with different data processing strategies (see Methods). 'GluAX-EM' particles are untagged subunits observed by cryo-EM. The subunit fractions from SiMPull experiments were calculated by probing immobilized hpAMPARs with a fluorescently-labeled, subunit-specific mAb. For SiMPull experiments, n = 120 images examined over two independent experiments. Data are represented as mean values +/− SEM.

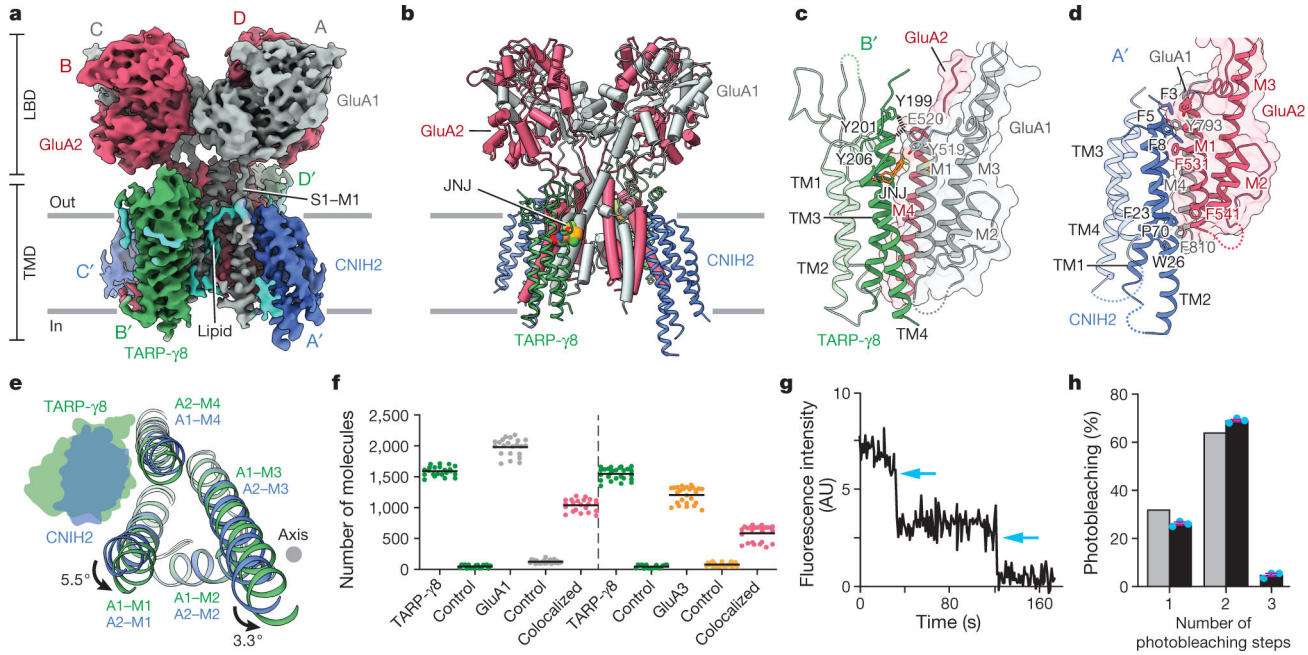

Figure 2. Architecture and subunit arrangement of the LBD-TMD$_{A1/A2}$ complex.

a. Three-dimensional reconstruction of LBD-TMD$_{A1/A2}$ complexes viewed parallel to the membrane. GluA1, GluA2, TARP-γ8, and CNIH2 are grey, red, green, and blue, respectively. Lipid-like densities are in cyan.

b. The structures of LBD-TMD$_{A1/A2}$ complexes viewed parallel to the membrane. The JNJ molecule is in sphere representation.

c. Interface between TARP-γ8 and receptor. Selected residues along the interface are shown as sticks. Possible hydrogen-bonds are indicated as black dashed lines.

d. Interface between CNIH2 and receptor, highlighting key residues.

e. Superimposition of the TARP-γ8 interface (**c**) and CNIH2 interface (**d**) to show the conformational differences in the A’ and B’ positions, viewed perpendicular to the membrane. For clarity, the solvent accessible surfaces of TARP-γ8 and CNIH2 are shown.

f. Observed colocalization of TARP-γ8 with GluA1 (65%) and colocalization of GluA3 with TARP-γ8 (38%) from SiMPull experiments. See Methods for description of control experiments. N= 25 images examined over two independent experiments.

g. Representative trace showing two-step photobleaching (blue arrows) of the 13A8 GFP-tagged anti-TARP-γ8 Fab.

h. Summary of photobleaching step distribution for the 13A8 GFP-tagged anti-TARP-γ8 Fab. The photobleaching step distribution for anti-TARP-γ8 Fab (black bars) is consistent with a binomial distribution (grey bars) that assumes a dimeric protein and 80% GFP maturation. N = 600 spots were analyzed from three photobleaching movies (200 spots/movie) collected from two independent experiments. Each movie is represented by a blue dot. Data are represented as mean values +/− SEM.

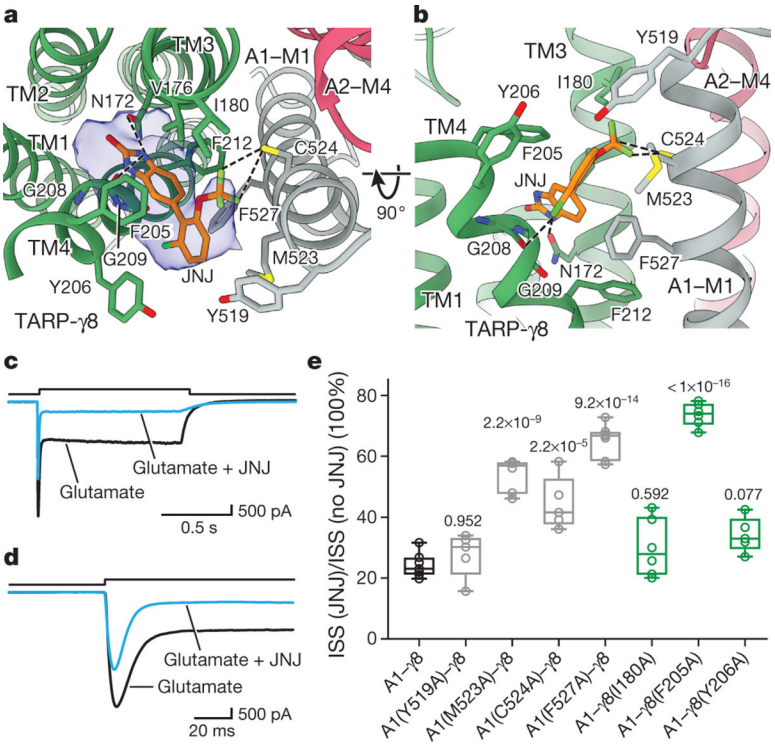

Figure 3. JNJ binding site and mechanism of inhibition

a-b. JNJ density and binding site viewed from the extracellular side (**a**) and parallel to the membrane (**b**). JNJ density is shown as a partially transparent blue surface. Possible hydrogen-bonds are indicated as black dashed lines.

c-d. Current responses of GluA1-TARP-γ8 complexes evoked by glutamate and glutamate plus JNJ (cyan trace) at a time scale of 500 ms (**c**) and 20 ms (**d**), taken after steady-state responses reached a plateau.

e. Box plot showing the extent of JNJ-induced steady-state current reduction from wild type and mutants (n=7 (wild type, A1-F527A/γ8), n=6 (A1-M523A/γ8, A1/γ8-I180A, A1/γ8-F205A) and n=5 (A1-Y519A/γ8, A1-C524A/γ8, A1/γ8-Y206A)). Boxes show the 25th and 75th percentiles, and whiskers down to the minimum and up to maximum values. The horizontal line in each box shows the median value. A one-way analysis of variance with Sidak's multiple comparison test was used to determine the significance and p values are indicated above the boxes. No adjustment was applied for multiple comparison.

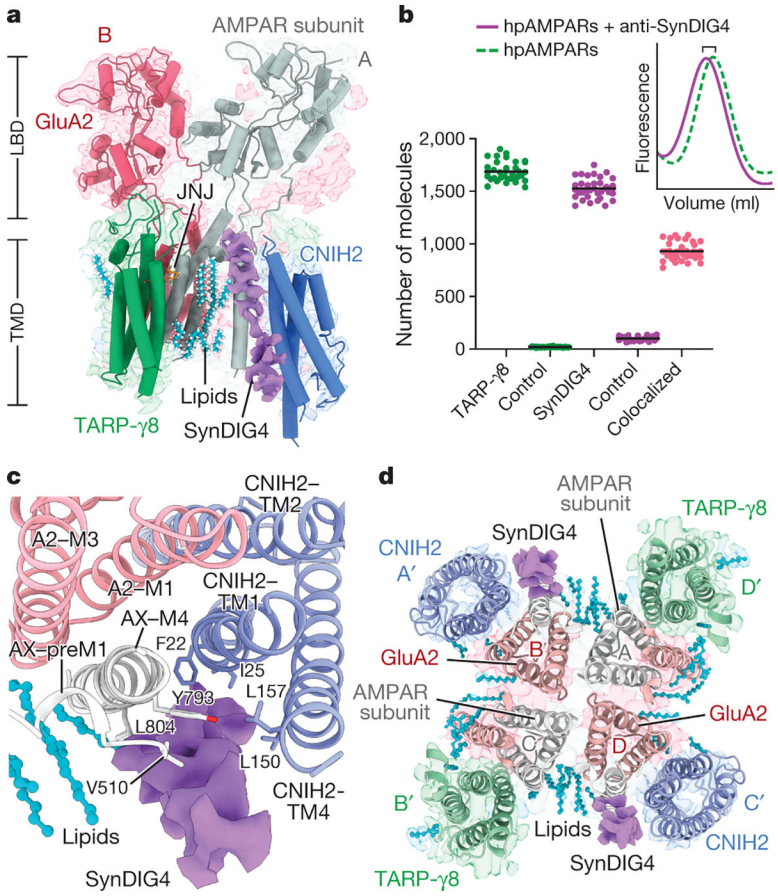

Figure 4. Elucidation of putative SynDIG4 density and interaction sites

a. The LBD-TMD$_{mix}$ reconstruction viewed parallel to the membrane. For clarity, only two AMPAR subunits are displayed in each panel. Cryo-EM density for SynDIG4 is shown in purple. Lipids are displayed in cyan. GluA2, TARP-γ8 and CNIH2 are red, green, and blue, respectively. AMPAR subunits in positions A (grey) and C (not shown) are undetermined.

b. Observed colocalization of SynDIG4 with TARP-γ8 (61%) from SiMPull experiments. See Methods for description of control experiments. Inset: The dotted line represents the chromatography profile of hpAMPARs incubated with the anti-TARP-γ8 Alexa647-labeled 13A8 mAb. The solid line represents the profile of the hpAMPARs incubated with the Alexa647-labeled 13A8 mAb and the anti-SynDIG4 mAb. A shift in size represents detection of SynDIG4 from the hpAMPARs.

c. Putative interaction sites of SynDIG4 with CNIH2 and an undetermined AMPAR subunit(s). View is perpendicular to the membrane. Red model = GluA2. Grey model = an undetermined AMPAR subunit (AX).

d. Top down view perpendicular to the membrane displaying the overall stoichiometry and arrangement of the TMD layer. Cryo-EM density for putative SynDIG4 is opaque, density for all other proteins is transparent.